

Volume-conserving *trans-cis* isomerization pathways in photoactive yellow protein visualized by picosecond X-ray crystallography

Yang Ouk Jung, Jae Hyuk Lee, Joonghan Kim, Marius Schmidt, Keith Moffat,
Vukica Šrajer, Hyotcherl Ihee*

* To whom correspondence should be addressed. E-mail : hyotcherl.ihee@kaist.ac.kr

This PDF file includes:

Supplementary Methods

Supplementary Tables S1-S10

Supplementary Figures S1-S14

Supplementary References

Supplementary Movies S1-S4

Supplementary Methods

Data collection protocol

Wild-type PYP (WT-PYP) and the E46Q mutant were expressed, purified, and crystallized at pH 7.0 as described previously¹⁻³. WT- and E46Q- PYP crystals, typically larger than $\sim 400 \mu\text{m}$ (length) $\times 100 \mu\text{m}$ (width) $\times 100 \mu\text{m}$ (thickness), were mounted in 0.7-mm diameter glass #50 capillaries (Hampton Research) and used for time-resolved crystallography studies at beamline ID09B at the European Synchrotron Radiation Facility (ESRF) and at BioCARS beamline 14-IDB at the Advanced Photon Source (APS). WT-PYP data were collected at both ESRF (in October 2004, May 2005, October 2005, October 2006, and October 2007) and APS (in August 2008 and November 2008), and E46Q-PYP data were collected only at APS (in November 2008, July 2009, December 2009, March 2010, July 2010, and July 2011). Time-resolved Laue diffraction images were acquired using the pump-probe method: a laser pulse triggered a photochemical reaction in a PYP crystal (pump) and a time-delayed X-ray pulse produced a diffraction pattern on a Mar165 CCD detector (probe). The data at ESRF has a smaller number of time delays but higher signal to noise ratio at each time delay as a result of averaging multiple data sets. On the other hand, the data at APS has a larger number of time delays more suitable for kinetic analysis. As shown later, both ESRF and APS data for WT-PYP show consistent reaction pathways and intermediates with some differences in the reaction rates, which are due to the sparse number of time-points in the ESRF data as well as experimental condition such as temperature.

For the experimental setup at the ID09B beamline at ESRF, the laser pulse as pump was stretched to ~ 100 ps, a duration that is long compared to the excited state lifetime. Thus, the pCA chromophore can be excited several times during each excitation pulse, providing multiple

opportunities to generate the photoproduct and increase its yield. The excitation pulse was generated by frequency-doubling 800-nm pulses produced in a customized, amplified Ti:Sapphire femtosecond laser system (Spectra Physics, Hurricane). The 400-nm, ~ 120 fs pulses were routed through two 15-cm long fused silica rods, which stretched the pulses to ~ 0.5 ps. These stretched pulses were focused into the 200- μm core of a 3-m long multi-mode optical fiber. Modal dispersion in the optical fiber further stretched the pulses to ~ 100 ps. Stimulated Raman scattering in the optical fiber, an unavoidable consequence arising from the high peak power of the optical pulses, broadened and shifted the laser spectrum to 418 nm. An asymmetric optical relay imaging system was used to focus the laser pulse to an elliptical spot (typically 0.12×0.24 mm²) along a path orthogonal to the X-ray beam. The laser energy measured at the sample location was about 40 μJ . After the laser pulse triggered a reaction in the single crystal, a time-delayed ~ 150 -ps X-ray probe pulse from the ESRF synchrotron was delivered to the crystal. Single PYP crystals were mounted in sealed capillaries of 0.7 mm diameter and the data were collected at 25 °C. To maximize the number of X-ray photons in a single probe pulse, the experiment was scheduled when ESRF operated in a rare 4-bunch mode (~ 2 weeks per year). In this mode, four equidistant bunches are separated by 705 ns, the bunch current is 10 mA and the pulse length is ~ 150 ps (FWHM). The wavelength of the X-ray pulse spanned the range from ~ 0.77 to 1.24 Å, and a single pulse delivered about 10^{10} photons to the sample. The X-rays were produced by a 236-pole in-vacuum undulator with a magnetic period of 17 mm. The undulator was operated with a 6.0 mm gap where the fundamental energy was ~ 15 keV with a 3% bandwidth. The white X-ray beam was focused into a 0.10×0.06 mm² focal spot by a toroidal mirror with an energy cut-off at 27 keV. Single pulses of X-rays were selected by a chopper rotating at ~ 1 kHz, the 360th sub-harmonic of the orbit frequency. The chopper defined an open

window of 500 ns centered on the selected pulse. Finally, a pulsed millisecond shutter isolated, on demand, single pulses from the ~ 1 kHz pulse train from the chopper.

For the experimental setup at the 14-IDB beamline at APS, a single PYP crystal was excited by ~ 35 ps laser pulses at 390 nm (for WT-PYP) or 500 nm (for E46Q-PYP) generated by the picosecond laser system⁴. A femtosecond pulse train at 780 nm was generated from a Spectra-Physics Tsunami Ti:sapphire laser oscillator and used to seed the picosecond amplifier system (Spectra-Physics Spitfire Pro). The output from the amplifier was sent to a TOPAS optical parametric amplifier to generate broadly tunable wavelength output. Pulses from the TOPAS were stretched to ~ 35 ps by an echelon. The ~ 110 μJ laser pulses were focused to an elliptical spot of 0.6×0.1 mm^2 size at the sample, yielding a power density of 2.5 mJ/mm^2 . The laser beam was perpendicular to the X-ray beam⁴. Single PYP crystals were mounted in sealed capillaries of 0.7 mm diameter and were maintained at 15 °C by a temperature controlled nitrogen stream (Oxford Cryostream). Time-resolved data were collected in the hybrid mode of the APS storage ring. In this mode a single 16 mA bunch is separated from adjacent septuplets by 1.59 μs . The single bunch in this mode has fourfold larger electron charge than a single bunch in the standard, 24-bunch operating mode⁴. To maximize the flux of single ~ 100 ps X-ray pulses, two collinear 2.4 m undulators with periods of 23 mm and 27 mm were used⁴. The gap of each undulator was adjusted such that the energies of both first harmonics peaked at 12 keV. The 100-ps (FWHM) X-ray pulse containing $\sim 4 \times 10^{10}$ photons was focused by Kirkpatrick-Baez focusing mirrors, trimmed by slits and delivered to the sample at a spot size of 0.09×0.06 mm^2 (horizontal \times vertical, FWHM). Single X-ray pulses were isolated from the high-frequency pulse train by a series of synchronized shutters: high-heat-load chopper, a Jülich high-speed chopper and a millisecond shutter⁴. The high-heat-load chopper, positioned upstream of the rest to reduce

the heat-load at the high-speed chopper, produced 22 μ s X-ray bursts at 82.3Hz. A downstream millisecond shutter isolated on demand a single burst of the high-heat-load chopper. A single X-ray pulse from this single X-ray burst was isolated by the high-speed Jülich chopper where a triangular-shaped rotor with a tunnel rotates at \sim 1 kHz, a subharmonic of the synchrotron, and results in an open window of \sim 210 ns.

For all experiments on WT-PYP and E46Q-PYP, the pump-probe cycle was repeated at 0.5 Hz and 1 Hz, respectively, typically 4–8 times prior to the detector readout. This provides sufficient time for the pCA chromophore to return to its ground state following the photo-initiation and for the gas stream to extract laser-induced excess heat from the crystal. As mentioned above, the laser beam illuminated the crystal along the path that was perpendicular to the X-ray beam⁴. The width of the elliptical laser spot size exceeded the horizontal X-ray beam size and its length (along the X-ray beam) exceeded the thickness of the crystals and therefore the path length of the X-ray beam through the crystal. Due to high optical density of the crystals at the wavelength used, the penetration depth of the laser pulse is quite shallow, less than 10 μ m^{5,6}, which required precise positioning of the crystal at the intersection of the laser and X-ray beams. Diffraction data were acquired in such a way that images were recorded at a particular crystal orientation at all desired time delays, before rotating the crystal to a new angular setting. Numerous orientations, each of which sampled a different region of reciprocal space, were acquired from a single rod-shaped PYP crystal. Making the time delay the fast variable in the data collection strategy minimizes a systematic error between time points that might otherwise arise from crystal-to-crystal variation and/or radiation damage^{6,7}. To minimize radiation damage and retain high-resolution reflections, the crystal was translated to illuminate a fresh spot after being exposed to between 500 and 1300 X-ray pulses. The time series consisted of a negative time

point (-20 ns), laser-off time point, and several positive time points. The measured time delays are distributed nearly evenly in logarithmic time, as follows: 0 ps, 100 ps, 316 ps, 1 ns, 3.16 ns, 10 ns, and 1 μ s for WT-PYP at ESRF; 100 ps, 178 ps, 316 ps, 562 ps, 1 ns, 1.78 ns, 3.16 ns, 5.62 ns, 10 ns, 100 ns, and 1 μ s for WT-PYP at APS; 100 ps, 178 ps, 316 ps, 562 ps, 1 ns, 1.78 ns, 3.16 ns, 5.62 ns, 10 ns, 17.8 ns, and 31.6 ns for E46Q mutant at APS. The negative time point places the probe X-ray pulse ahead of the pump laser pulse, and ensures that the wait time between laser pulses (2 sec for WT-PYP and 1 sec for E46Q mutant) was sufficient to fully recover the PYP dark state. At the laser-off time point, images were collected without a pump pulse, after PYP recovery time. The nominal 0 ps time delay corresponds to maximal overlap of the pump and probe pulses.

Data processing, data averaging, and visualization of difference density maps

The Laue data reduction procedures used in this work are described elsewhere⁸⁻¹¹. Data statistics including redundancy and completeness are summarized in Supplementary Table 1-3. The data are highly redundant and the resolution cutoff extends below 1.6 Å. We note that the signal-to-noise ratio of the present data is of high quality compared with previous time-resolved Laue crystallographic data, based on the resolution and completeness of the last shell^{8,12,13}. Indexing, integration, scaling, and merging of all data sets was performed with *LaueView*⁹ and yielded the structure factor amplitudes ($|F(hkl, t)|$) and the associated errors ($\sigma(hkl)$) for each reflection and time point. The values of $|F(hkl, reference)|$ were used to represent the amplitude of the dark state. The reference time point corresponds to a negative time delay (-20 ns for WT-PYP at ESRF and E46Q-PYP at APS) or a laser-off condition (for WT-PYP at APS). The time-dependent difference structure factor amplitudes were obtained by scaling to calculated

(absolute) amplitudes from the ground state structure (F_c^{dark}) and by subtraction: $\Delta F(hkl, t) = |F(hkl, t)| - |F(hkl, \text{reference})|$. Weighted difference structure factor amplitudes were generated by scaling $\Delta F(hkl, t)$ by a weight factor $w(hkl) = 1/(1+(\Delta F(hkl)^2/\langle \Delta F^2 \rangle) + (\sigma(hkl)^2/\langle \sigma^2 \rangle))^{14}$. Weighting down observations with higher experimental error¹⁰ enhances the signal-to-noise ratio of electron density maps constructed from the experimental structure factor amplitudes. Weighted difference structure factors ($w(hkl) \cdot \Delta F(hkl, t)$) from different volumes on the same crystal and when needed from multiple crystals were merged to produce a single, highly redundant and complete data set at each time point. Before merging all observations in reciprocal space, some data sets with low signal-to-noise ratio (SNR) were omitted according to their quality factors. The quality factors¹¹ were evaluated in the following way. First, experimental, weighted difference electron density maps $\Delta\rho(t)$ were generated by Fourier transformation of each set of $w \cdot \Delta F(hkl, t)$ with phases calculated from the PYP model of the dark state. This procedure employs the difference-Fourier approximation¹⁵. Then, the standard deviations of the difference density distribution were obtained over two spherical volumes of radius 5 Å, one centered on atom C1 of the pCA chromophore (assessing structural changes in the vicinity of the pCA chromophore, thereby representing “signal”) and the other on atom CD2 of Trp119 (which remains stationary upon isomerization, thereby representing “noise”). The signal-to-noise quality factor was then calculated as the ratio of these two standard deviations¹¹. The merged difference electron density maps $\Delta\rho(t)$ generated with this procedure are shown in Supplementary Figs. S1~S3. Supplementary Fig. S1a, S2a, and S3a show both the whole protein view and the chromophore binding pocket view of WT-ESRF, WT-APS, and E46Q-APS, respectively (WT-ESRF; WT-PYP data collected at ESRF, WT-APS; WT-PYP data collected at APS, E46Q-APS; E46Q-PYP data collected at APS). Supplementary Figs. S1b, S2b, and S3b show thresholdless

maps for the front and side views of the chromophore binding pocket of WT-ESRF, WT-APS, and E46Q-APS, respectively (see also Fig 2 and Supplementary Movies S1~S3). These time-resolved, color-coded electron density maps are generated by superimposing experimentally-determined, thresholdless electron density maps for the ground state (magenta) and the photoproduct state (green) at each time point¹⁶. Where there is no structural change, the magenta and green maps blend to white; where electron density is displaced, the direction of atomic motion is indicated by a magenta-to-green color gradient.

Singular value decomposition (SVD) analysis

To identify the kinetic mechanism and structures of intermediates during the early times of the PYP photocycle, we extracted time-independent difference electron densities from the time-dependent densities representing the mixtures of states at each time point, by using the SVD method^{8,12,17}. In detail, an $M \times N$ data matrix \mathbf{A} was first constructed from M grid points of difference electron densities for each of the N time points. These M grid points covered the whole PYP molecule at 2-sigma level. For the data presented in this paper, the values of M and N are typically $\sim 31,000$ and 11, respectively. Then, the method of SVD was used to decompose the \mathbf{A} matrix ($M \times N$) into a product of three matrices according to $\mathbf{A} = \mathbf{U} \cdot \mathbf{S} \cdot \mathbf{V}^T$, where \mathbf{U} represents the left singular vectors (ISVs), \mathbf{S} contains the singular values, and \mathbf{V} represents the right singular vectors (rSVs). The $M \times N$ matrix \mathbf{U} contains N ISVs which are time-independent difference electron density maps, each of which has M grid points; the $N \times N$ matrix \mathbf{V} contains N rSVs representing the time-dependencies of the corresponding ISVs; and the rank-ordered singular values along the diagonal \mathbf{S} matrix ($N \times N$) describe the relative contribution of each ISV to the data matrix \mathbf{A} . Since the diagonal elements (i.e. singular values) of \mathbf{S} are ordered so

that $s_1 \geq s_2 \geq \dots \geq s_n \geq 0$, ISV and rSV are ordered in terms of their relative contribution to the experimental data. Only the first few SVs contribute to the structures of reaction intermediates, others contain only noise. To assess which vectors are dominated by noise, we used visual inspection of ISVs, the singular values and the autocorrelation factors¹⁷. Only the first three of the eleven ISVs have significant singular values and positive auto-correlation factors for WT-APS (Supplementary Fig. S5a, S5b, and S5c; see also Supplementary Figs. S4 and S6 for WT-ESRF and E46Q-APS, respectively). Linear combinations of these ISVs reproduced the experimental data with high fidelity (Supplementary Fig. S5d)¹⁸. Thus, these three SVs were selected for further kinetic analysis. The corresponding rSVs multiplied by the corresponding singular values for these three components were globally fitted with a sum of two single exponential functions, for which the least-squares relaxation times were 1 ± 0.2 ns and 36 ± 10 ns for WT-APS (Supplementary Fig. S5e) and 0.5 ± 0.4 ns and 1.6 ± 1.5 ns for WT-ESRF. In the case of E46Q data, the first two ISVs have significant singular values and the corresponding first two rSVs were globally fitted with a single exponential function with a relaxation time of 14 ± 1 ns.

To extract the time-independent difference electron density maps, we performed kinetic analysis using a simple 3-state sequential model for WT (2-state sequential model for E46Q) as follows. New \mathbf{U}' , \mathbf{V}' and \mathbf{S}' matrices can be defined by removing non-significant components from \mathbf{U} , \mathbf{V} and \mathbf{S} , respectively. In other words, \mathbf{U}' is an $M \times 3$ matrix (or $M \times 2$ matrix for E46Q) which contains first three (or two for E46Q) left singular vectors, \mathbf{S}' is a 3×3 (or 2×2 for E46Q) diagonal matrix which contains first three (or two for E46Q) singular values, and \mathbf{V}' is an $N \times 3$ matrix (or $N \times 2$ matrix for E46Q) which contains first three (or two for E46Q) right singular vectors. The three (or two for E46Q) rSVs (\mathbf{V}') can be transformed into time-dependent

population changes (\mathbf{C}') of three (or two for E46Q) intermediates using a parameter matrix (\mathbf{P}) that satisfies $\mathbf{V}' = \mathbf{C}'\mathbf{P}$. Once \mathbf{C}' is specified by a kinetic model with a certain set of kinetic parameters such as rate coefficients, \mathbf{P} can be obtained by minimizing the discrepancy between \mathbf{V}' and $\mathbf{C}'\mathbf{P}$ by a least squares method (Supplementary Fig. S4f). Since $\mathbf{V}' = \mathbf{C}'\mathbf{P} \cong \mathbf{C}\mathbf{P}$, the following relationships hold:

$$\mathbf{A}' = \mathbf{U}'\mathbf{S}'\mathbf{V}'^T = \mathbf{U}'\mathbf{S}'(\mathbf{C}\mathbf{P})^T = \mathbf{U}'\mathbf{S}'(\mathbf{P}^T\mathbf{C}^T) = (\mathbf{U}'\mathbf{S}'\mathbf{P}^T)\mathbf{C}^T = \mathbf{F}\mathbf{C}^T$$

where \mathbf{A}' is $M \times N$ matrix which contains the theoretical difference density maps at given grid points and time points, and \mathbf{F} is $M \times 3$ (or $M \times 2$ matrix for E46Q) matrix which contains time-independent difference density maps that were made by linear combination of first three (or two for E46Q) singular vectors (singular value-weighted left singular vectors). Once the \mathbf{P} matrix is determined, the time-independent difference density maps can be expressed as a linear combination of the first three left singular vectors via $\mathbf{F} = \mathbf{U}'\mathbf{S}'\mathbf{P}^T$.

Assuming a simple sequential kinetic pathway involving three states for WT-PYP (or two states for E46Q-PYP), three (or two for E46Q) time-independent electron density maps for three (or two for E46Q) intermediates can be constructed from simple linear combinations of the three ISVs components with the refined time constants, 1.7 ± 0.6 ns and 40 ± 8 ns for WT-APS (Supplementary Fig. S5e and S5f) or 0.2 ± 0.1 ns and 2 ± 1 ns for WT-ESRF (Supplementary Fig. S4e and S4f). In the analysis of E46Q-PYP, a simple sequential pathway connecting two states was assumed, and two time-independent maps could be constructed with a time constant 14 ± 1 ns (Supplementary Fig. S6). The time-independent difference maps recovered from this SVD analysis (Supplementary Fig. S7 for WT-ESRF, see also Supplementary Fig. S8 for WT-APS, and Supplementary Fig. S9 for E46Q-APS) were used to refine the time-independent structures shown in Supplementary Figs. S7~S9, whose refinement statistics are summarized in

Supplementary Table 4~6 (see the next section for details).

Generating extrapolated maps and structure refinement

Refinement procedures used in this work are described elsewhere^{12,19,20}. All refinements and the model building were performed with SHELX-97²¹ and XtalView²² (Supplementary Figs. S7~S9). 5% of the total reflections were used to calculate a free R-factor. The refinement of intermediate structures was performed against the structure factor amplitudes that had been extrapolated to 100% photoactivation (extrapolated structure factor amplitudes). These extrapolated structure factor amplitudes were generated by first Fourier transforming the time-independent difference maps recovered from the SVD analysis to yield time-independent difference structure factors $\Delta F^{ind}(hkl)$ for each intermediate. Extrapolated structure factor amplitudes F^{extr} were then calculated as $F^{extr}(hkl) = F_{calc}^{dark}(hkl) + (2/p) \cdot w(hkl) \cdot \Delta F^{ind}(hkl)$ ¹² from which extrapolated maps can also be calculated, using the dark PYP structure to calculate phases. The factor p represents the extent of photoactivation. Its optimum value eliminates the contribution of the “dark” state to the time-resolved, experimentally determined electron density maps¹². Features suitable to assess the extent of photoactivation include the negative density on atom O4 of the chromophore and on residues Tyr42, Glu46, and Arg52. The factor p is typically 0.05. Initially, rigid body refinement was performed while the coordinates of the chromophore and other residues remained fixed. Restraints for distance, angle, and planarity in the chromophore were gradually relaxed to enable highly distorted, non-planar structures such as the chromophore of the I_T intermediate to be refined in the absence of normal stereochemical restraints.

The structures of intermediates were refined against the time-independent, extrapolated structure factor amplitudes. In case of WT-PYP, the first of the three extrapolated maps is structurally

homogeneous; i.e. it is well modeled by a single structure (I_T). The second map is structurally heterogeneous, suggesting a mixture of two distinct intermediate structures, and refinement employed a mixture of two structures ($I_{CT} + pR_1$). We also tested other models in which we attempted to fit the extrapolated data with a single structure of I_{CP} , I_{CT} , or pR_1 . The residual maps show that the mixture of I_{CT} and pR_1 is the best model for the second map (Supplementary Fig. S11). The third map is also structurally heterogeneous and was refined using a mixture of pR_1 and pR_2 . Despite the heterogeneous nature of these maps, the values of R- (R-free) factor and diffraction-data precision index (DPI)²³ in Supplementary Table 4 (for WT-ESRF) and Supplementary Table 5 (for WT-APS) represent a good quality of the structure refinement. We note that the structures of the three intermediates from APS and ESRF data are consistent. In the case of E46Q-PYP, the first and the second extrapolated maps are structurally homogeneous, and were refined with I_T and pR_1 , respectively (Supplementary Table 6). Selected structural parameters for the stable, dark state and all transient intermediates for WT-ESRF, WT-APS, and E46Q-APS are shown in Table 1, Supplementary Table 7 and Supplementary Table 8, respectively.

Posterior Analysis

In order to explore kinetic mechanisms consistent with our data, posterior analysis^{8,17} was applied with time-independent difference density maps, which were derived from previously refined intermediate structures (I_T , I_{CT} , pR_1 , and pR_2). In posterior analysis, theoretical time-dependent difference electron density maps were calculated based on parameters of the chosen mechanism such as the number of intermediates, number of relaxations, and pathways by which intermediates form and decay. Since the kinetic mechanism was affected by the instrument

response function (IRF) in the early time points such as 0 ps and 100 ps in the case of WT-ESRF, the theoretical model for posterior analysis is convoluted with a function describing the X-ray temporal profile (a Gaussian function with 164 ps full width at half maximum at ESRF). The estimated extent of photoinitiation (~ 0.05) is also determined by scaling experimental density maps to theoretical density maps at the first three time points. This is consistent with the factor p for extrapolating difference density maps. Since we determined the time-independent mixture of these two structures (I_{CT} and pR_1) from structure refinement of the second time-independent map, we explored a bifurcation mechanism for WT-PYP in which the first intermediate, I_T , converts into I_{CT} and pR_1 (and subsequently I_{CT} further converts to pR_2). The fit between these calculated difference density maps and the experimental difference density maps resulted in three associated time constants; 1.7 ± 0.5 ns (k_1), 3 ± 1 ns (k_2) and 20 ns \pm 7 ns (k_3) for WT-APS, or 0.4 ± 0.1 ns (k_1), 0.7 ± 0.2 ns (k_2) and 6 ± 1 ns (k_3) for WT-ESRF. We note that the same reaction mechanism and the same intermediates explain the data from both APS and ESRF although the reaction rates are faster for the ESRF data due to higher sample temperature. In the case of E46Q-PYP, a simple mechanism of I_T to pR_1 gave a satisfactory fit with time constant of 11 ± 0.1 ns. The reaction rates are summarized in Supplementary Table 9.

To test the quality of this proposed mechanism, we checked several other candidate mechanisms, optimized rate constants, and calculated the magnitude of total squared deviation between the calculated and experimental maps. We then compared these values for the proposed mechanism and the other candidate mechanisms. Indeed, other candidate mechanisms result in the increase of magnitude of total squared deviation. In addition, another mechanism was tested, derived from a previous time-resolved X-ray Laue crystallography⁸ study. In that mechanism, I_T is converted to a single structure (I_{CP} or I_{CT}) instead of bifurcating into a mixture of I_{CT} and pR_1 and the I_{CP}

(or I_{CT}) bifurcates into pR_1 and pR_2 . This mechanism could not fit the experimental data satisfactorily. In the previous time-resolved Laue crystallography⁸ study, the time resolution was a few nanoseconds and the earliest time delay was 1 ns. Thus I_T structure could not be captured and the density map at 1 ns was assigned to a single structure called I_{CP} . As shown in Supplementary Fig. S11, I_{CP} structure alone cannot explain the second time-independent density map whereas $I_{CT} + pR_1$ accounts for the map satisfactorily.

Computational details of DFT calculations

Density functional theory (DFT) calculations were performed to assess the nature of the intermediate I_T . Since calculating the whole PYP molecule is computationally impractical, a model system containing only 157 atoms was employed; these included the pCA chromophore and eight residues surrounding the chromophore (Cys69, Tyr42, Glu46, Thr50, Arg52, Ala67, Thr70, and Phe96). The boundaries of the model system were set by (i) truncating the peptide bond (C–N) and adding O^- (making $-COO^-$) or H_2^+ (making $-NH_3^+$) or (ii) truncating the C–C bond and adding H (making $-CH_3$). In this way, all necessary hydrogen bonds are retained and the overall charge on these residues is the same in the model as in the whole protein. Since hydrogen bonds between the pCA and the residues as well as among the residues themselves need to be considered, it is essential to choose an appropriate DFT functional. We used the B97-1 hybrid functional²⁴, which is known to give accurate results for hydrogen-bonded and weakly interacting systems²⁵. To speed up the calculations, 6-31G(d) basis sets were used for the pCA chromophore while 3-21G basis sets were used for the protein residues. The experimental coordinates of the residues determined from the structure refinement were used as a starting point in the DFT calculation. The positions of one or two carbon atoms in each residue (except

Cys69) were fixed (the coordinates of eight carbon atoms in total) during geometry optimization to avoid disintegration of the model system. Geometry optimizations and subsequent vibrational frequency calculations were carried out using the Gaussian03 program²⁶. The coordinates of the final optimized geometry are listed in Supplementary Table 10.

From the number of imaginary frequencies recovered in the calculations, one can infer the nature of the molecular structure. For example, zero, one, and two or more imaginary frequencies generally indicate a local minimum, a transition state, or a higher saddle point, respectively²⁷. The I_T structure has no imaginary frequency. The harmonic vibrational frequency analysis confirmed that the I_T structure is a local minimum. When only three residues (Cys69, Tyr42, Glu46) instead of eight or no residues were included, we could not find a local minimum corresponding to I_T.

Supplementary References

- 1 Imamoto, Y., Ito, T., Kataoka, M. & Tokunaga, F. Reconstitution photoactive yellow protein from apoprotein and p-coumaric acid derivatives. *FEBS Lett.* **374**, 157-160, (1995).
- 2 McRee, D. E. *et al.* Crystallographic structure of a photoreceptor protein at 2.4 Å resolution. *Proc. Natl. Acad. Sci. U. S. A.* **86**, 6533-6537, (1989).
- 3 Devanathan, S., Lin, S., Cusanovich, M. A., Woodbury, N. & Tollin, G. Early intermediates in the photocycle of the Glu46Gln mutant of photoactive yellow protein: femtosecond spectroscopy. *Biophys. J.* **79**, 2132-2137, (2000).
- 4 Graber, T. *et al.* BioCARS: a synchrotron resource for time-resolved X-ray science. *J. Synchrotron Radiat.* **18**, 658-670, (2011).
- 5 Ng, K., Getzoff, E. D. & Moffat, K. Optical studies of a bacterial photoreceptor protein, photoactive yellow protein, in single crystals. *Biochemistry* **34**, 879-890, (1995).
- 6 Schmidt, M., Srajer, V., Purwar, N. & Tripathi, S. The kinetic dose limit in room-temperature time-resolved macromolecular crystallography. *J. Synchrotron Rad.* **19**, 264-273, (2012).
- 7 Ren, Z. *et al.* Laue crystallography: coming of age. *J. Synchrotron Radiat.* **6**, 891-917, (1999).
- 8 Ihee, H. *et al.* Visualizing reaction pathways in photoactive yellow protein from nanoseconds to seconds. *Proc. Natl. Acad. Sci. U. S. A.* **102**, 7145-7150, (2005).
- 9 Ren, Z. & Moffat, K. Quantitative Analysis of Synchrotron Laue Diffraction Patterns in Macromolecular Crystallography. *J. Appl. Crystallogr.* **28**, 461-481, (1995).
- 10 Ursby, T. & Bourgeois, D. Improved Estimation of Structure-Factor Difference

- Amplitudes from Poorly Accurate Data. *Acta Crystallogr.* **A53**, 564-575, (1997).
- 11 Rajagopal, S., Schmidt, M., Anderson, S., Ihee, H. & Moffat, K. Analysis of experimental time-resolved crystallographic data by singular value decomposition. *Acta Crystallogr.* **D60**, 860-871, (2004).
- 12 Schmidt, M. *et al.* Protein kinetics: structures of intermediates and reaction mechanism from time-resolved x-ray data. *Proc. Natl. Acad. Sci. U. S. A.* **101**, 4799-4804, (2004).
- 13 Knapp, J. E., Pahl, R., Srajer, V. & Royer, W. E., Jr. Allosteric action in real time: time-resolved crystallographic studies of a cooperative dimeric hemoglobin. *Proc. Natl. Acad. Sci. U. S. A.* **103**, 7649-7654, (2006).
- 14 Ren, Z. *et al.* A molecular movie at 1.8 Å resolution displays the photocycle of photoactive yellow protein, a eubacterial blue-light receptor, from nanoseconds to seconds. *Biochemistry* **40**, 13788-13801, (2001).
- 15 Henderson, R. & Moffat, J. K. The difference Fourier technique in protein crystallography: errors and their treatment. *Acta Crystallogr.* **B27**, 1414-1420, (1971).
- 16 Schotte, F., Soman, J., Olson, J. S., Wulff, M. & Anfinrud, P. A. Picosecond time-resolved X-ray crystallography: probing protein function in real time. *J. Struct. Biol.* **147**, 235-246, (2004).
- 17 Schmidt, M., Rajagopal, S., Ren, Z. & Moffat, K. Application of singular value decomposition to the analysis of time-resolved macromolecular x-ray data. *Biophys. J.* **84**, 2112-2129, (2003).
- 18 Henry, E. R. The use of matrix methods in the modeling of spectroscopic data sets. *Biophys. J.* **72**, 652-673, (1997).
- 19 Anderson, S. *et al.* Chromophore conformation and the evolution of tertiary structural

- changes in photoactive yellow protein. *Structure* **12**, 1039-1045, (2004).
- 20 Terwilliger, T. C. & Berendzen, J. Bayesian difference refinement. *Acta Crystallogr.* **D52**, 1004-1011, (1996).
- 21 Sheldrick, G. M. A short history of SHELX. *Acta Crystallogr.* **A64**, 112-122, (2008).
- 22 McRee, D. E. XtalView/Xfit--A versatile program for manipulating atomic coordinates and electron density. *J. Struct. Biol.* **125**, 156-165, (1999).
- 23 Cruickshank, D. W. Remarks about protein structure precision. *Acta Crystallogr. D* **D55**, 583-601, (1999).
- 24 Hamprecht, F. A., Cohen, A. J., Tozer, D. J. & Handy, N. C. Development and assessment of new exchange-correlation functionals. *J. Chem. Phys.* **109**, 6264-6271, (1998).
- 25 Sousa, S. F., Fernandes, P. A. & Ramos, M. J. General performance of density functionals. *J. Phys. Chem. A* **111**, 10439-10452, (2007).
- 26 Gaussian 03, Revision C.02 (2004).
- 27 Cramer, C. J. *Essentials of computational chemistry: theories and models.* (Wiley, 2004).
- 28 Kleywegt, G. J. Use of non-crystallographic symmetry in protein structure refinement. *Acta Crystallogr.* **D52**, 842-857, (1996).
- 29 The PyMOL Molecular Graphics System (DeLano Scientific LLC, San Carlos, CA, USA., 2003).

Supplementary Table S1. Crystallographic data statistics of averaged datasets for WT-PYP collected at ESRF.

Time Point	0 ps	100 ps	316 ps	1 ns	3.16 ns	10 ns
Individual Datasets (#)	2	11	8	9	4	4
Total observations	89396	854375	624704	716506	276490	268838
Unique observations	12871	13925	13844	13859	13539	13353
Redundancy	6.95	61.35	45.12	51.70	20.42	20.13
R_{merge} on $ F ^2$ (%) ^a	12.51 ~ 14.41	10.50 ~ 13.79	10.33 ~ 17.85	9.21 ~ 14.67	11.84 ~ 17.98	11.24 ~ 18.07
R_{merge} on $ F $ (%) ^b	8.75 ~ 9.03	6.67 ~ 10.38	6.67 ~ 11.48	5.86 ~ 9.57	7.55 ~ 11.48	7.28 ~ 11.54
Completeness (%)						
100 to 1.6 Å	90.15	99.78	99.34	99.48	97.48	96.19
Last shell (1.66~1.60 Å)	72.69	99.51	97.90	98.42	91.22	86.95

^a R_{merge} on $|F| = \sum||F| - \langle|F|\rangle| / \sum|F|$ where $\langle|F|\rangle$ is the mean amplitude of multiple observations and symmetry measurements. ^b R_{merge} on $|F|^2 = \sum||F|^2 - \langle|F|^2\rangle| / \sum|F|^2$ where $\langle|F|^2\rangle$ is the mean intensity of multiple observations and symmetry measurements.

Supplementary Table S2. Crystallographic data statistics of averaged datasets for WT-PYP collected at APS. Only a single data set was used in this case.

Time Point	100 ps	178 ps	316 ps	562 ps	1 ns	1.78 ns
Total observations	197133	205662	203967	198099	200087	190259
Unique observations	13308	13172	13404	13396	13241	13247
Redundancy	14.81	15.61	15.22	14.78	15.11	14.36
R _{merge} on F ² (%) ^a	14.83	18.12	17.67	17.64	18.09	15.83
R _{merge} on F (%) ^b	8.45	10.20	9.97	9.72	10.23	8.99
Completeness (%)						
100 to 1.6 Å	96.05	95.07	96.75	96.64	96.59	95.59
Last shell (1.66~1.60 Å)	86.08	82.40	88.11	87.24	83.95	82.89

Time Point	3.16 ns	5.62 ns	10 ns	100 ns	1 us
Total observations	196843	195908	184736	186841	187842
Unique observations	13350	13368	13322	13122	13301
Redundancy	14.74	14.66	13.86	14.24	14.12
R _{merge} on F ² (%) ^a	18.97	19.04	17.06	19.55	19.90
R _{merge} on F (%) ^b	10.60	10.71	11.47	11.09	11.15
Completeness (%)					
100 to 1.6 Å	96.33	96.44	96.15	94.71	96.02
Last shell (1.66~1.60 Å)	86.12	85.78	84.88	80.30	83.98

^a R_{merge} on |F| = $\frac{\sum||F| - \langle|F|\rangle|}{\sum|F|}$ where $\langle|F|\rangle$ is the mean amplitude of multiple observations and symmetry measurements. ^b R_{merge} on |F|² = $\frac{\sum||F|^2 - \langle|F|^2\rangle|}{\sum|F|^2}$ where $\langle|F|^2\rangle$ is the mean intensity of multiple observations and symmetry measurements.

Supplementary Table S3. Crystallographic data statistics of averaged datasets for E46Q-PYP collected at APS.

Time Point	100 ps	178 ps	316 ps	562 ps	1 ns	1.78 ns
Individual Datasets (#)	15	15	14	14	17	20
Total observations	1398775	1398595	1393460	1276570	1569471	1730305
Unique observations	13909	13909	13888	13884	13899	13873
Redundancy	100.57	100.55	100.34	91.94	112.92	124.72
R_{merge} on $ F ^2$ (%) ^a	8.08 ~ 22.57	12.61 ~ 22.73	11.67 ~ 23.79	11.69 ~ 23.90	11.82 ~ 23.85	10.82 ~ 24.12
R_{merge} on $ F $ (%) ^b	4.22 ~ 13.12	7.60 ~ 13.14	5.27 ~ 13.93	6.29 ~ 13.66	6.33 ~ 13.67	5.95 ~ 13.75
Completeness (%)						
100 to 1.6 Å	99.33	99.75	99.64	99.58	99.61	99.52
Last shell (1.66~1.60 Å)	99.09	99.02	98.53	98.04	98.23	97.86
Time Point	3.16 ns	5.62 ns	10 ns	17.8 ns	31.6 ns	
Individual Datasets (#)	14	14	13	8	6	
Total observations	1078030	1032245	1023384	539482	333568	
Unique observations	13844	13834	13835	13669	13645	
Redundancy	77.87	74.61	73.97	39.46	24.46	
R_{merge} on $ F ^2$ (%) ^a	10.94 ~ 23.75	10.86 ~ 24.02	12.57 ~ 25.32	12.57 ~ 18.22	12.57 ~ 17.24	
R_{merge} on $ F $ (%) ^b	5.96 ~ 13.63	5.91 ~ 13.80	7.47 ~ 15.09	7.47 ~ 10.42	7.47 ~ 9.82	
Completeness (%)						
100 to 1.6 Å	99.42	99.41	99.41	98.28	98.18	
Last shell (1.66~1.60 Å)	97.26	97.37	97.29	92.06	92.34	

^a R_{merge} on $|F| = \frac{\sum||F| - \langle|F|\rangle|}{\sum|F|}$ where $\langle|F|\rangle$ is the mean amplitude of multiple observations and symmetry measurements. ^b R_{merge} on $|F|^2 = \frac{\sum||F|^2 - \langle|F|^2\rangle|}{\sum|F|^2}$ where $\langle|F|^2\rangle$ is the mean intensity of multiple observations and symmetry measurements.

Supplementary Table S4. Refinement data statistics for time-independent intermediates for WT-PYP collected at ESRF.

Intermediate	I_T	$I_{CT} + pR_1$	$pR_1 + pR_2$
R_{work} (%)	22.48	22.26	22.68
R_{free}^a (%)	27.60	26.38	26.96
DPI ^b (Å)	0.114	0.207	0.209
B-factor (Å ²)	17.9	17.6	18.3
Solvent content ^c (%)	21.2	19.2	19.1

^a Calculated with 5% of random reflections excluded from refinement.

^b Diffraction Precision Index²³

^c The fraction of the unit cell volume not occupied by the model.

Supplementary Table S5. Refinement data statistics for time-independent intermediates for WT-PYP collected at APS.

Intermediate	I_T	$I_{CT} + pR_1$	$pR_1 + pR_2$
R_{work} (%)	25.95	32.63	31.61
R_{free}^a (%)	29.28	36.75	36.29
DPI ^b (Å)	0.105	0.229	0.225
B-factor (Å ²)	18.6	18.9	18.1
Solvent content ^c (%)	21.2	18.0	17.1

^a Calculated with 5% of random reflections excluded from refinement.

^b Diffraction Precision Index²³

^c The fraction of the unit cell volume not occupied by the model.

Supplementary Table S6. Refinement data statistics for time-independent intermediates for E46Q-PYP collected at APS.

Intermediate	I _T	pR ₁
R _{work} (%)	15.9	28.42
R _{free} ^a (%)	18.8	32.73
DPI ^b (Å)	0.07	0.118
B-factor (Å ²)	19.4	21.4
Solvent content ^c (%)	21.4	20.8

^a Calculated with 5% of random reflections excluded from refinement.

^b Diffraction Precision Index²³

^c The fraction of the unit cell volume not occupied by the model.

Supplementary Table S7. Geometrical parameters (distances, torsion angle and planarity angle) of the pCA chromophore in the ground state (pG) and intermediates (I_T, I_{CT}, pR₁, pR₂, and pB) for WT-PYP collected at ESRF.

	pG	I _T	I _{CT}	pR ₁	pR ₂	pB
O1-Cys69, Å	2.8	2.9	4.7	3.4	3.8	2.9
O4'-Tyr42, Å	2.5	2.6	2.3	2.9	2.9	5.0
O4'-Glu46, Å	2.6	2.7	2.9	5.1	3.3	7.8
C1-C2-C3-C1', °	169	89	-3	-1	-6	-24
Planarity angle, °	22	87	46	35	26	51

O1, the chromophore carbonyl oxygen; O4', the chromophore phenolate oxygen; Tyr42, the hydroxyl oxygen of Tyr42; Glu46, the Oε2 of Glu46; Cys69, the backbone amide nitrogen of Cys69; Planarity angle denotes the angle between the carbonyl bond (C1—O1) and the plane of the chromophore phenolate ring; the angle is 90 degrees when this bond is normal to the plane.

Supplementary Table S8. Geometrical parameters (distances, torsion angle and planarity angle) of the pCA chromophore in the ground state (pG) and intermediates (I_T, pR₁, and pB) for E46Q-PYP collected at APS.

	pG	I _T	pR ₁	pB
O1-Cys69, Å	2.8	3.0	3.4	2.9
O4'-Tyr42, Å	2.5	2.8	3.1	5.0
O4'-Glu46, Å	2.6	3.2	5.6	7.8
C1-C2-C3-C1', °	169	73	2	-24
Planarity angle, °	22	86	33	51

O1, the chromophore carbonyl oxygen; O4', the chromophore phenolate oxygen; Tyr42, the hydroxyl oxygen of Tyr42; Glu46, the Oε2 of Glu46; Cys69, the backbone amide nitrogen of Cys69; Planarity angle denotes the angle between the carbonyl bond (C1—O1) and the plane of the chromophore phenolate ring; the angle is 90 degrees when this bond is normal to the plane.

Supplementary Table S9. Summary of rate constants

	WT-ESRF	WT-APS	E46Q-APS
Model fitting on SVD			
1/k ₁	0.2 ± 0.1 ns	1.7 ± 0.6 ns	14 ± 1 ns
1/k ₂	2 ± 1 ns	40 ± 8 ns	—
Posterior Analysis			
1/k ₁ (I _T -to-I _{CT})	0.4 ± 0.1 ns	1.7 ± 0.5 ns	11 ± 0.1 ns
1/k ₂ (I _T -to-pR ₁)	0.7 ± 0.2 ns	3 ± 1 ns	—
1/k ₃ (I _{CT} -to-pR ₂)	6 ± 1 ns	20 ns ± 7 ns	—

Supplementary Table S10. The xyz coordinates of the optimized I_T structures from DFT calculation.

Atom type	X	y	z	
C	9.299023	-6.292268	-0.952140	FIX
C	8.497449	-4.988507	-0.721572	
C	9.114466	-3.757106	-0.424547	
C	8.374591	-2.574906	-0.238762	
C	7.090091	-4.979431	-0.799553	
C	6.343312	-3.810877	-0.610166	
C	6.963528	-2.564562	-0.331233	
O	6.221388	-1.406104	-0.218665	
C	8.702023	-0.325268	-4.376140	
C	8.072667	-1.649101	-3.876363	FIX
C	6.658259	-1.512286	-3.278502	
C	5.633325	-0.894531	-4.219473	
O	5.892781	-0.389574	-5.313650	
O	4.342337	-0.902820	-3.748772	
C	8.936342	0.755866	-3.262656	
O	8.041547	1.208802	-2.519769	
N	7.385823	3.580762	-1.003746	
C	5.934023	3.613732	-0.501140	FIX
C	5.352346	2.188089	-0.630919	
O	6.358521	1.333635	0.027347	
C	5.054984	1.805480	-2.086380	
C	6.058390	3.944029	1.022097	
O	4.957536	3.855098	1.658535	
N	8.593665	1.814532	2.059012	
C	8.783023	0.839732	3.184860	FIX
C	7.779829	-0.335089	3.183503	
C	6.440320	-0.037231	3.896604	
C	5.708526	1.197848	3.316061	
N	4.305103	1.196885	3.824098	
C	3.641023	2.270732	4.284860	FIX
N	4.067868	3.505154	4.025189	
N	2.526299	2.061088	5.041295	
C	10.235375	0.257131	2.998329	
O	10.880132	0.912958	2.018076	
C	-0.622386	-3.013664	2.729562	
C	-0.223977	-2.324268	1.389860	FIX
C	-2.108859	-2.844723	3.012195	
O	-2.993578	-3.448246	2.335006	

N	-2.478993	-2.017150	4.029741	
C	-1.586144	-1.108230	4.808501	
C	-3.875598	-1.995459	4.524172	
C	-3.751989	-1.287456	5.898465	
C	-2.604244	-0.274399	5.636534	
C	-4.874008	-1.228070	3.635797	
O	-6.082274	-1.203261	3.936706	
N	-4.338299	-0.626785	2.535708	
C	-5.215094	-0.099272	1.498958	
C	-4.939375	1.365691	1.118293	
S	-3.436138	1.822205	0.114378	
C	-5.255999	-0.998238	0.234213	
O	-5.683067	-0.547773	-0.848197	
C	-1.960857	1.443731	1.086338	
O	-1.860854	0.501591	1.866713	
C	-0.890042	2.448101	0.879562	
C	0.449358	2.245188	0.781373	
C	1.235902	1.055950	0.447801	
C	2.532818	0.920320	0.990514	
C	3.405265	-0.075154	0.561064	
C	3.059335	-0.895012	-0.541833	
C	1.745264	-0.803102	-1.054653	
C	0.850825	0.144095	-0.563127	
O	3.970095	-1.678225	-1.134246	
N	-4.843525	-2.274153	0.449937	
C	-4.807279	-3.253743	-0.646181	
C	-3.385664	-3.407411	-1.248216	
O	-2.445673	-4.071784	-0.346422	
C	-2.844977	-2.038268	-1.702140	FIX
C	0.013023	4.199732	-2.415140	FIX
C	0.090360	2.798871	-3.017872	
C	-1.077736	2.039117	-3.206892	
C	1.324110	2.243281	-3.400668	
C	-1.011771	0.760626	-3.777911	
C	1.401197	0.960694	-3.960775	
C	0.225483	0.221614	-4.157181	
H	10.374173	-6.100447	-0.856382	
H	9.016412	-7.054156	-0.213815	
H	10.197491	-3.712085	-0.331856	
H	6.563184	-5.906497	-1.016678	
H	8.891110	-1.645297	-0.016211	
H	5.260433	-3.850152	-0.683150	
H	8.715572	-2.105484	-3.111144	

H	8.026596	-2.319998	-4.745946
H	6.689562	-0.927872	-2.353387
H	6.314630	-2.513686	-2.985163
H	8.008614	0.087277	-5.117653
O	10.203965	1.163406	-3.240672
H	4.425936	2.198274	-0.052563
H	4.552840	0.837657	-2.140602
H	4.376423	2.546847	-2.527580
H	5.974867	1.735473	-2.671385
H	6.321694	0.341179	-0.220411
H	5.342691	4.352010	-1.045228
H	7.658207	2.616841	-1.348795
H	7.578717	4.274362	-1.736720
O	7.233884	4.204912	1.442987
H	8.280974	-1.169392	3.690590
H	7.574570	-0.642430	2.146685
H	6.606030	0.113432	4.972599
H	5.793675	-0.920767	3.776285
H	6.173208	2.128848	3.653185
H	5.718517	1.187256	2.220625
H	3.800702	0.315846	3.741316
H	3.697858	4.277075	4.573344
H	4.589144	3.720503	3.092818
H	2.340863	1.154915	5.455256
H	1.831163	2.789968	5.149858
H	8.758975	1.363430	4.150025
H	8.304035	2.764161	2.325468
H	7.927793	1.485940	1.340690
H	10.082562	1.570337	1.690226
O	10.664790	-0.678799	3.672673
H	0.842893	-2.480163	1.196053
H	-0.419797	-1.250303	1.434217
H	-0.803514	-2.777461	0.575119
H	-0.017945	-2.638472	3.560862
H	-3.454888	-2.007928	6.670308
H	-4.702876	-0.821407	6.170664
H	-2.163265	0.124512	6.555323
H	-2.979998	0.549002	5.016847
H	-0.927277	-1.687559	5.469775
H	-0.999215	-0.487442	4.125044
H	-4.258720	-3.018296	4.603716
H	-3.480776	-4.064147	-2.124411
H	-2.666006	-1.407933	-0.822802

H	-1.893340	-2.170628	-2.230204
H	-3.568633	-1.525116	-2.346397
H	-2.694930	-3.882934	0.608393
H	-5.489070	-2.886294	-1.420343
H	-4.416151	-2.541186	1.339563
H	-0.834921	4.276024	-1.724057
H	0.932773	4.439225	-1.866343
H	-2.039026	2.444511	-2.900452
H	2.235949	2.813345	-3.240370
H	-1.922540	0.184157	-3.911493
H	2.367424	0.517745	-4.193533
H	0.276559	-0.773172	-4.590007
H	-6.223220	-0.128032	1.944180
H	-4.956398	1.988641	2.018111
H	-5.743614	1.675593	0.440665
H	2.885452	1.654119	1.713393
H	4.413060	-0.156921	0.957726
H	1.463966	-1.432179	-1.894631
H	-0.118072	0.250653	-1.045333
H	5.023179	-1.572702	-0.653883
H	-5.152654	-4.224299	-0.270011
H	-0.450410	-4.093643	2.632416
H	-3.329768	-0.557482	2.387069
H	1.055465	3.151728	0.881366
H	-1.244925	3.477974	0.903134
H	4.225298	-1.317096	-2.825283
H	7.884002	3.839659	-0.085374
N	10.070126	-0.540923	-4.970816
H	10.431285	-1.478871	-4.761072
H	10.096313	-0.372481	-5.981083
H	10.613813	0.535374	-4.033925
H	9.103392	-6.694089	-1.955272
H	-0.119309	4.952677	-3.205415

Supplementary Figure captions

Supplementary Figure S1. (a) Whole protein and chromophore binding pocket views of WT-ESRF difference electron density maps at 0 ps, 100 ps, 316 ps, 1 ns, 3.16 ns, 10 ns, and 1 μ s (ESRF data). All density maps are contoured as $+2\sigma$ (cyan), $+3\sigma$ (blue), -2σ (pink), and -3σ (red). (b) The front view and the side view of the WT-PYP thresholdless electron density maps (same data as in a) for the chromophore binding pocket. These time-resolved magenta-green maps are generated by superimposing experimentally-determined thresholdless electron density maps¹⁶ for the ground state (magenta color) and the photoproduct state (green color) at each time point. Magenta and green blend to white; thus, the appearance of color indicates structural change, and the direction of molecular motion follows the magenta-to-green color gradient (see also Supplementary Movie 1).

Supplementary Figure S2. (a) Whole protein view and chromophore binding pocket view of WT-APS difference electron density maps at 100 ps, 178 ps, 316 ps, 562 ps, 1 ns, 1.78 ns, 3.16 ns, 5.62 ns, 10 ns, 100 ns and 1 μ s. (b) The front view and the side view of the WT-APS thresholdless electron density maps in the chromophore binding pocket are also presented. All color schemes are identical to Supplementary Fig. S1. (see also Supplementary Movie S2).

Supplementary Figure S3. (a) Whole protein view and chromophore binding pocket view of E46Q-APS difference electron density maps at 100 ps, 178 ps, 316 ps, 562 ps, 1 ns, 1.78 ns, 3.16 ns, 5.62 ns, 10 ns, 17.8 ns, and 31.6 ns. (b) The front view and the side view of the E46Q-APS thresholdless electron density maps in the chromophore binding pocket are also presented. All

color schemes are identical to Supplementary Fig. S1. (see also Supplementary Movie S3).

Supplementary Figure S4. (a~c) Difference density maps of first four ISVs obtained by SVD analysis against WT-ESRF density maps. All density maps are contoured as $+3\sigma$ (violet), $+4\sigma$ (purple), -3σ (white), and -4σ (red). (d) The magnitude of singular value and its autocorrelation factors. Based on visual inspection of ISVs, the singular values and the autocorrelation factors, first three SVs have significant signal. (e) The first three rSVs fitting with a simple kinetic pathway. The refined time constants are ~ 200 ps and ~ 2 ns. (f) The first three rSVs fitting with a simple kinetic pathway involving three states can be transformed into time-dependent population changes of three intermediates. The refined time constants are ~ 200 ps and ~ 2 ns.

Supplementary Figure S5. (a~c) Difference density maps of first four ISVs obtained by SVD analysis against WT-APS density maps. All color schemes are identical to Supplementary Fig. S4. (d) The magnitude of singular value and its autocorrelation factors. Based on visual inspection of ISVs, the singular values and the autocorrelation factors, the first three SVs have significant signal. (e) The first three rSVs as fit with a simple kinetic pathway. The refined time constants are 1.7 ns and 40 ns. (f) The first three rSVs fitting with a simple kinetic pathway involving three states can be transformed into time-dependent population changes of three intermediates. The refined time constants are 1.7 ns and 40 ns.

Supplementary Figure S6. (a, b) Difference density maps of first three ISVs obtained by SVD analysis against E46Q-APS density maps. All color schemes are identical to Supplementary Fig. S4. (c) The magnitude of singular value and its autocorrelation factors. Based on visual

inspection of ISVs, the singular values and the autocorrelation factors, first two SVs have significant signal. **(d)** The first two rSVs fitting with a simple kinetic pathway. The refined time constants are 14 ns. **(e)** The first two rSVs fitting with a simple kinetic pathway involving three states can be transformed into time-dependent population changes of three intermediates. The refined time constant is 14 ns.

Supplementary Figure S7. Difference electron density maps of time-independent intermediates obtained by the SVD analysis against WT-ESRF density maps. The map for intermediate 1 **(a, d)** is consistent with the structural change of I_T from pG, the map for intermediate 2 **(b, e)** is for the structural change of I_{CT} and pR₁ mixture, and the map for intermediate 3 **(c, f)** is for the structural change of pR₁ and pR₂ mixture. All density maps are contoured as $+3\sigma$ (violet), $+4\sigma$ (purple), -3σ (white), and -4σ (red). Chromophore binding views of the refined time-independent intermediates with its extrapolated **(g, h, i)** and residuals map **(j, k, l)**. The color scheme for the intermediates follows that of Fig. 3. The refined structure of intermediate 1 is identified with I_T , and that of intermediate 2 is with the mixture of I_{CT} and pR₁, and that of intermediate 3 is with the mixture of pR₁ and pR₂.

Supplementary Figure S8. Difference electron density maps of time-independent intermediates obtained by the SVD analysis against WT-APS density maps. The map for intermediate 1 **(a, d)** is consistent with the structural change of I_T from pG, the map for intermediate 2 **(b, e)** is for the structural change of I_{CT} and pR₁ mixture, and the map for intermediate 3 **(c, f)** is for the structural change of pR₁ and pR₂ mixture. Chromophore binding views of the refined time-independent intermediates with its extrapolated **(g, h, i)** and residuals map **(j, k, l)**. All color

schemes are identical to Supplementary Fig. S7. The refined structure of intermediate 1 is identified with I_T , and that of intermediate 2 is with the mixture of I_{CT} and pR_1 , and that of intermediate 3 is with the mixture of pR_1 and pR_2 .

Supplementary Figure S9. Difference electron density maps of time-independent intermediates obtained by the SVD analysis against E46Q-APS density maps. The map for intermediate 1 (**a**, **c**) is consistent with the structural change of I_T from pG , the map for intermediate 2 (**b**, **d**) is for the structural change of pR_1 . Chromophore binding views of the refined time-independent intermediates with its extrapolated (**e**, **f**) and residuals map (**g**, **h**). All color schemes are identical to Supplementary Fig. S7. The refined structure of intermediate 1 is identified with I_T , and that of intermediate 2 is with pR_1 .

Supplementary Figure S10. Chromophore binding pocket views of superimposed intermediate structures with the ground state structure (gray) at (**a**) I_T (orange) (**b**) I_{CT} (cyan) (**c**) pR_1 (blue), and (**d**) pR_2 (green). The hydrogen bonding networks for intermediate are shown as red dashed line.

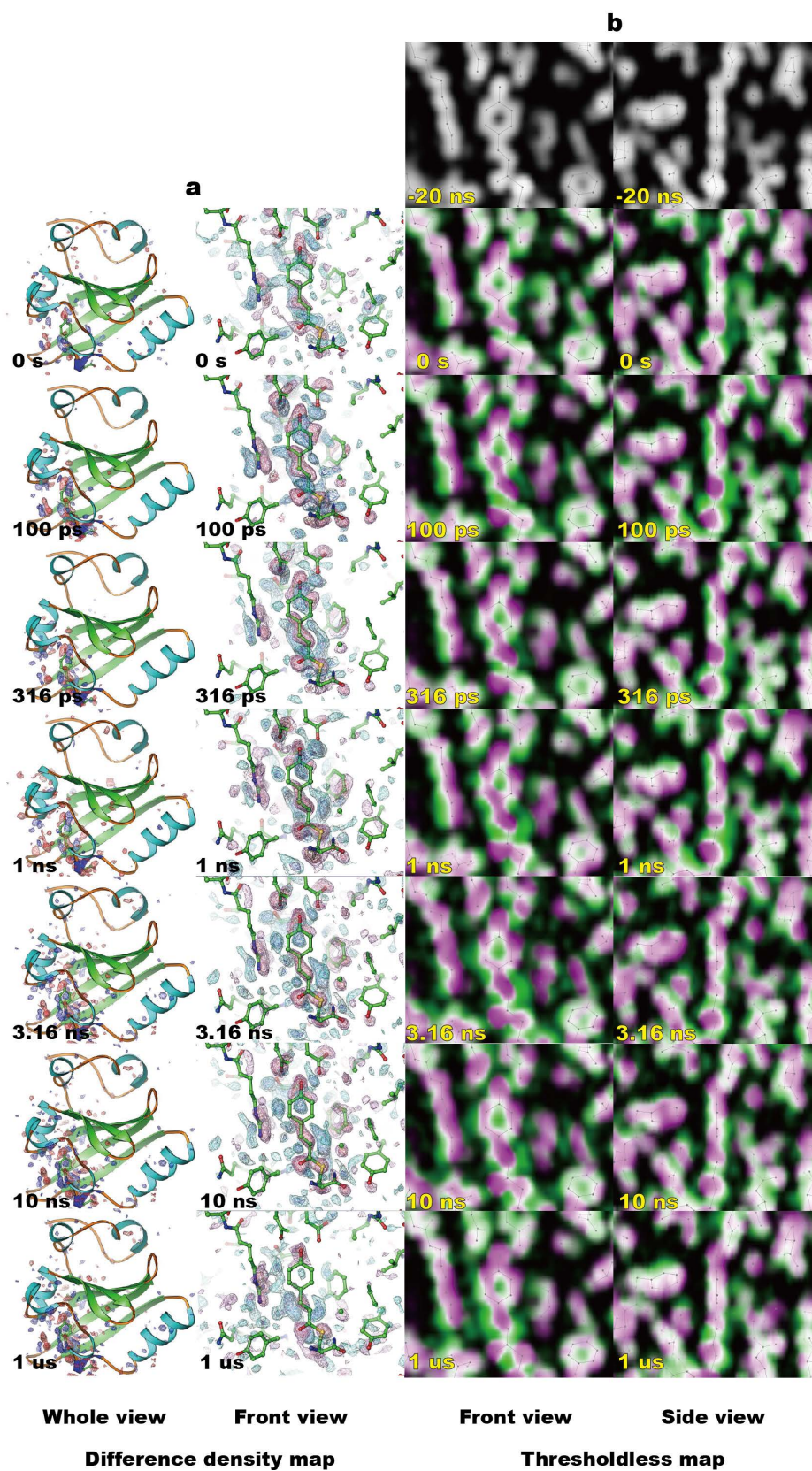
Supplementary Figure S11. Residual density maps of 2nd intermediate after refinement with the mixture of I_{CT} and pR_1 (**a**, **b**), I_{CP} (**c**, **d**), I_{CT} (**e**, **f**), and pR_1 (**g**, **h**). Front views (**a**, **c**, **e**, **g**) and side views (**b**, **d**, **f**, **h**) of chromophore binding pocket are shown. Residual densities in the cases of I_{CP} , I_{CT} , and pR_1 (**c** ~ **h**) support that the model of the mixture of I_{CT} and pR_1 (**a**, **b**) fully interpret electron density. All density maps are contoured as $+3\sigma$ (violet), $+4\sigma$ (purple), -3σ (white), and -4σ (red).

Supplementary Figure S12. Comparison of experimental difference electron density maps (WT-ESRF) and the calculated difference electron density maps based on the refined structures and the final reaction mechanism. Chromophore binding pocket views of experimental difference electron density maps at 0 ps, 100 ps, 316 ps, 1 ns, 3.16 ns, 10 ns, and 1 μ s (ESRF data for wild type) are shown in the left side and the calculated maps are shown in the right side. All density maps are contoured as $+2\sigma$ (cyan), $+3\sigma$ (blue), -2σ (pink), and -3σ (red).

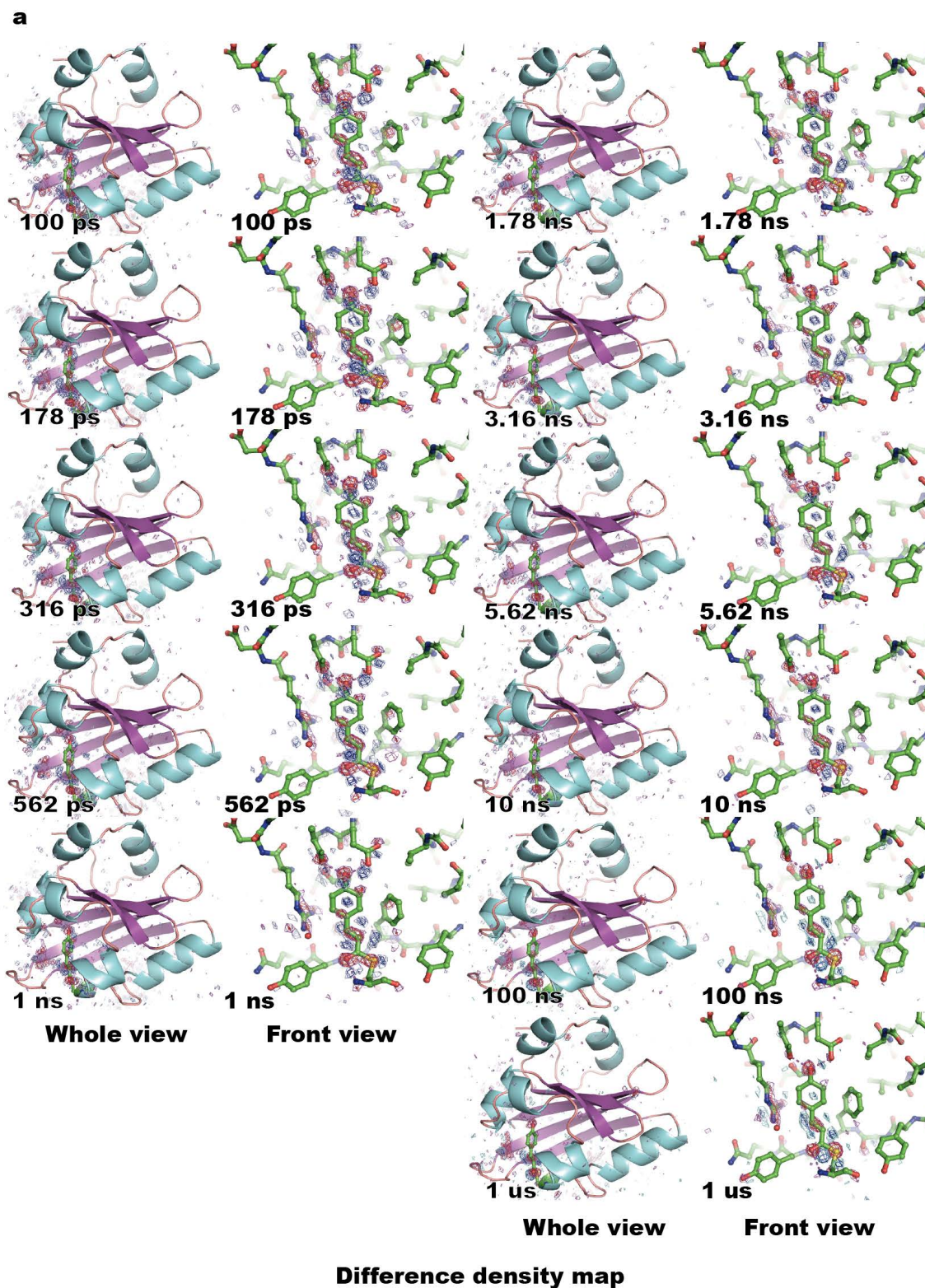
Supplementary Figure S13. Comparison of experimental difference electron density maps (WT-APS) and the calculated difference electron density maps based on the refined structures and the final reaction mechanism. Chromophore binding pocket views of experimental difference electron density maps at 100 ps, 178 ps, 316 ps, 562 ps, 1 ns, 1.78 ns, 3.16 ns, 5.62 ns, 10 ns, 100 ns and 1 μ s (APS data for wild type) are shown in the left side and the calculated maps are shown in the right side. All density maps are contoured as $+2\sigma$ (cyan), $+3\sigma$ (blue), -2σ (pink), and -3σ (red).

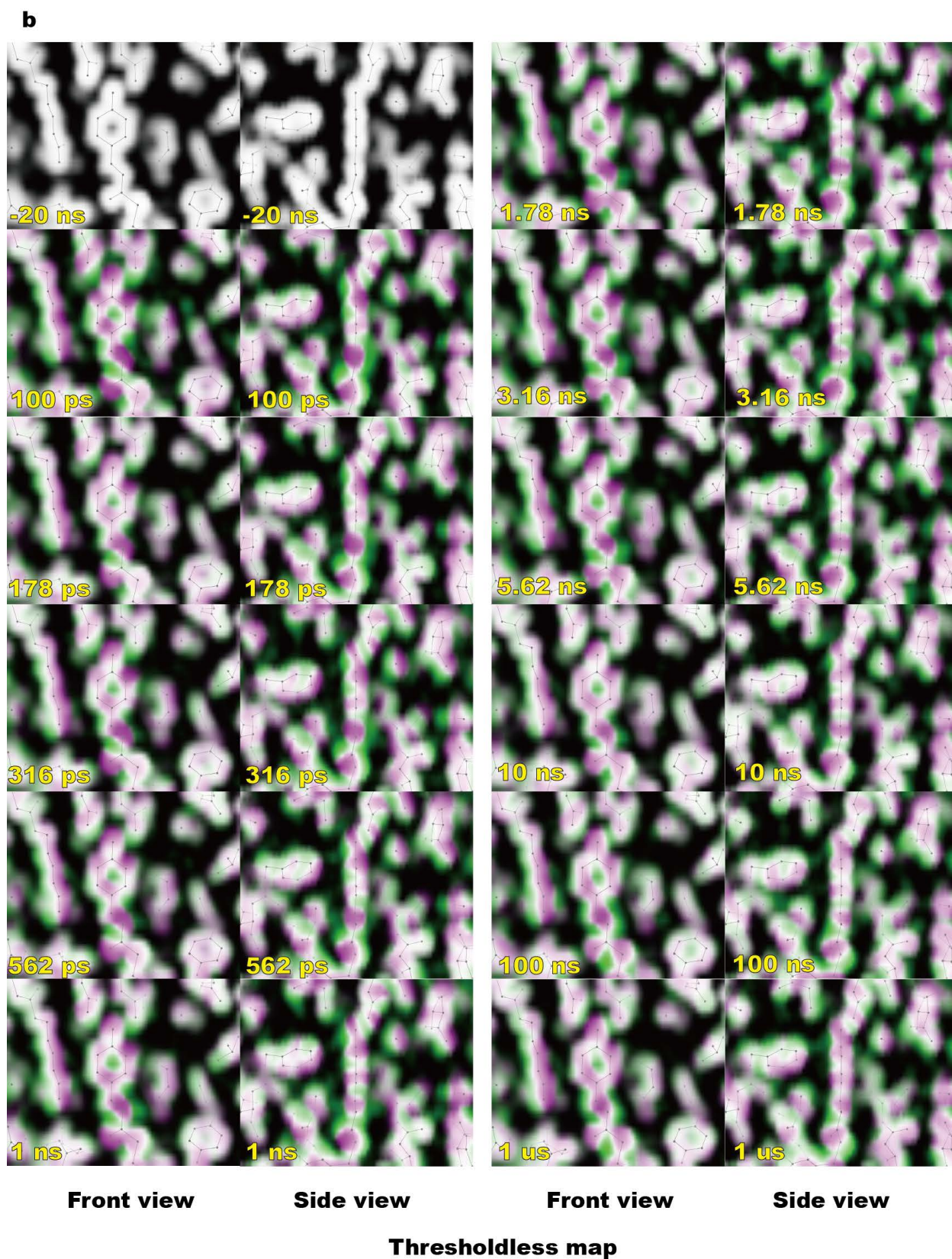
Supplementary Figure S14. Comparison of experimental difference electron density maps (E46Q-APS) and the calculated difference electron density maps based on the refined structures and the final reaction mechanism. Chromophore binding pocket views of experimental difference electron density maps at 100 ps, 178 ps, 316 ps, 562 ps, 1 ns, 1.78 ns, 3.16 ns, 5.62 ns, 10 ns, 17.8 ns, and 31.6 ns (APS data for E46Q mutant) are shown in the left side and the calculated maps are shown in the right side. All density maps are contoured as $+2\sigma$ (cyan), $+3\sigma$ (blue), -2σ (pink), and -3σ (red).

Supplementary Figure S1.

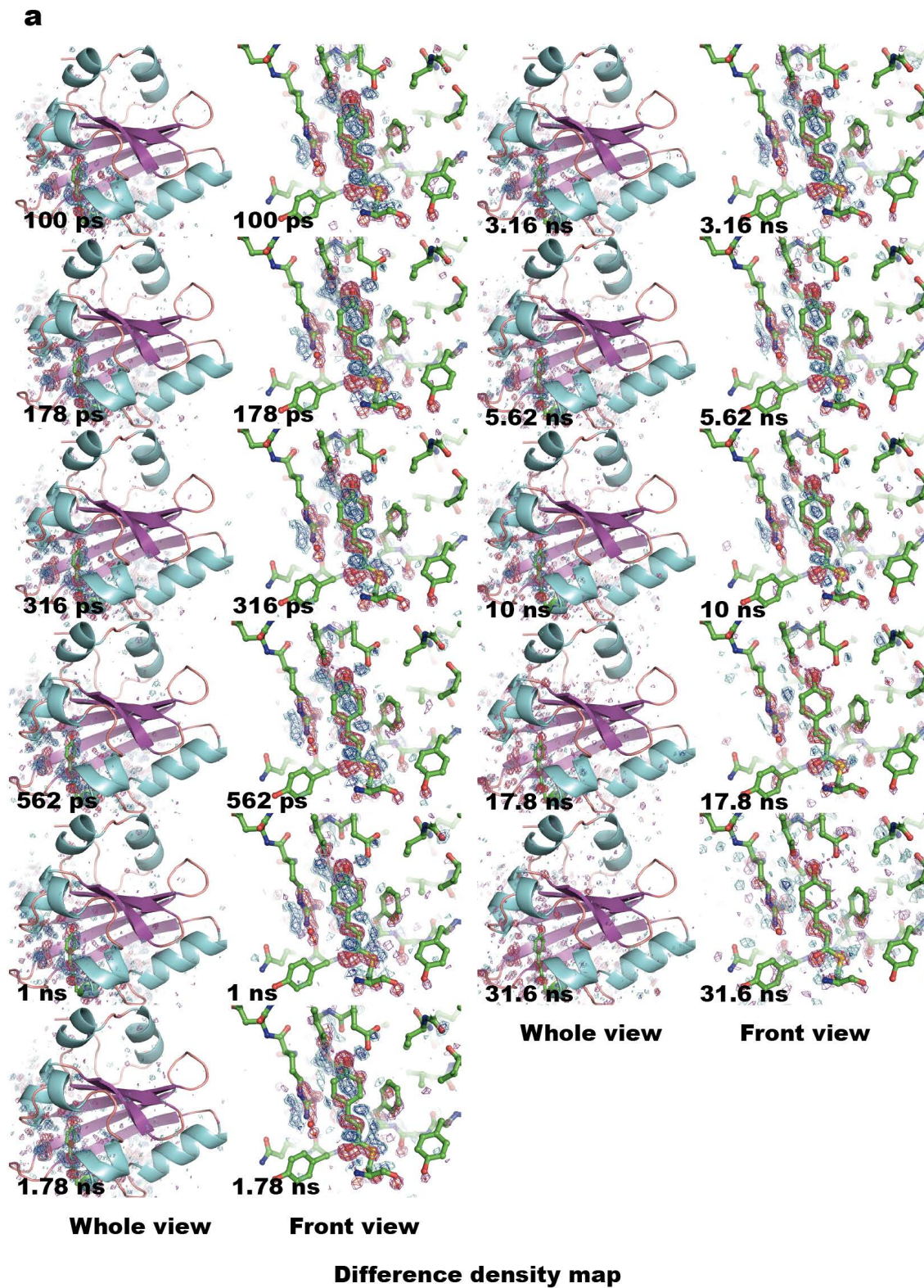


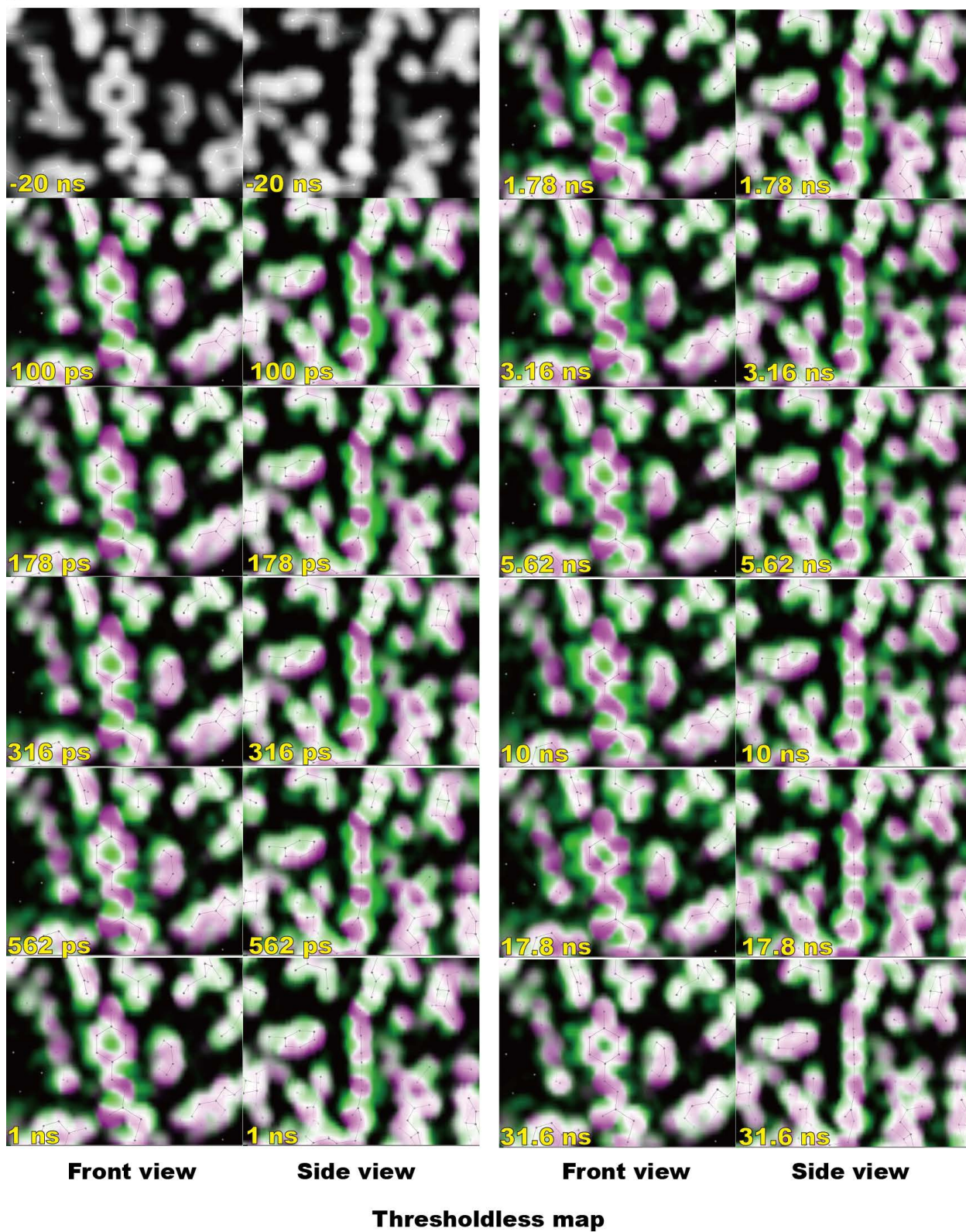
Supplementary Figure S2.



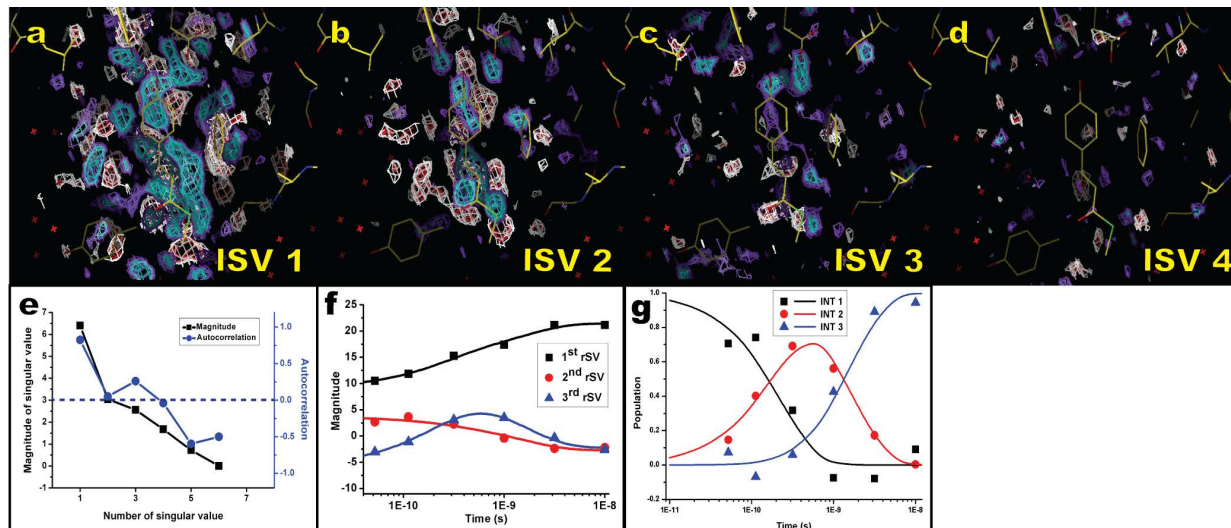


Supplementary Figure S3.

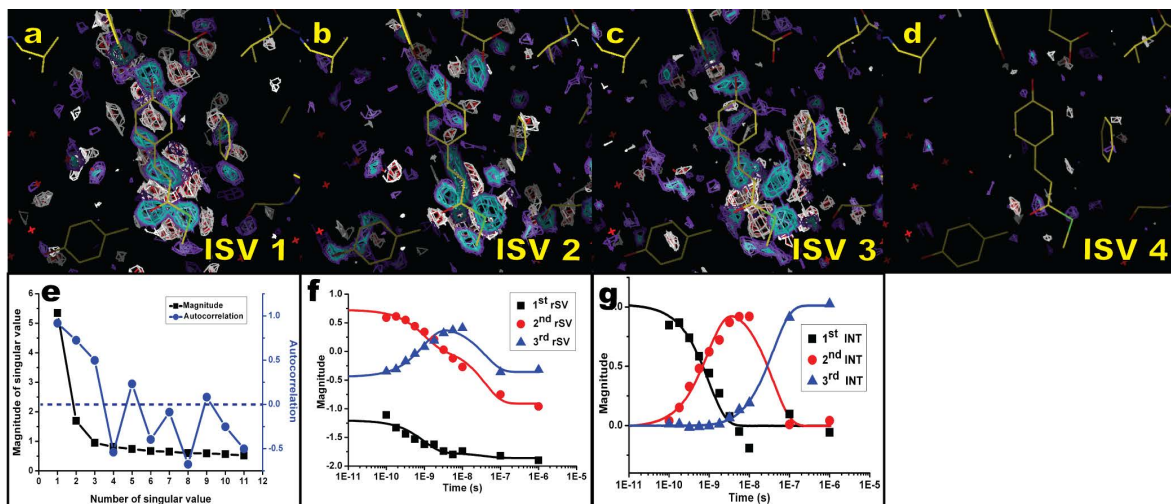


b

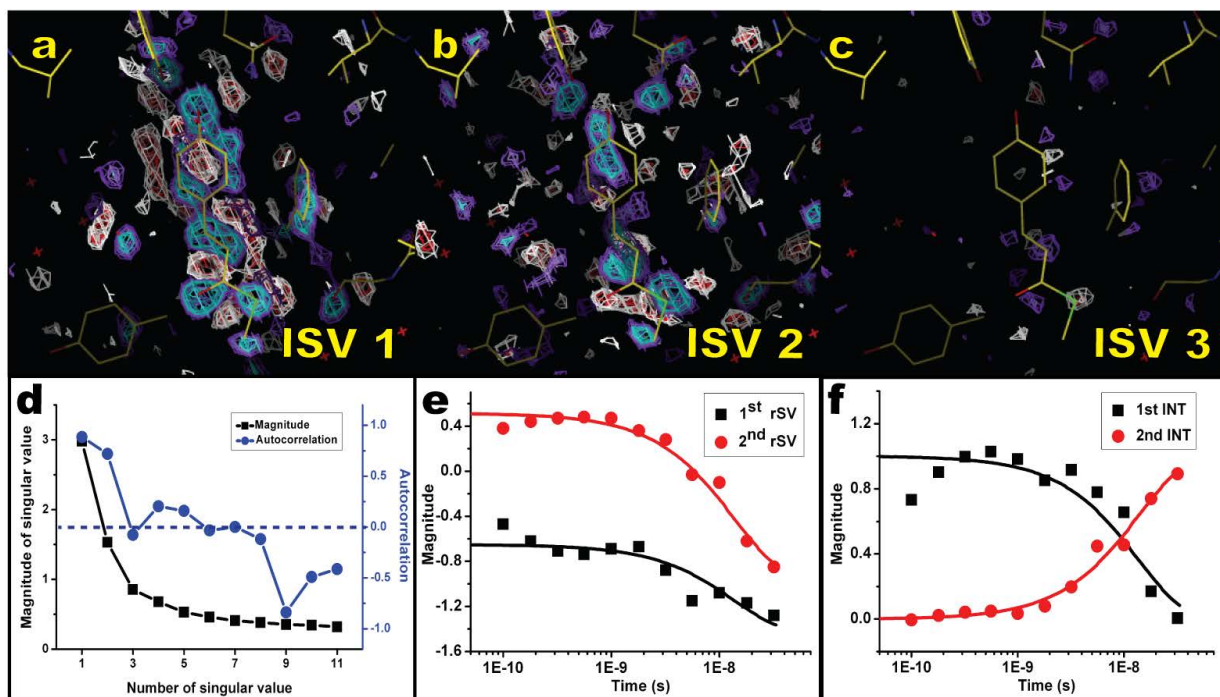
Supplementary Figure S4.



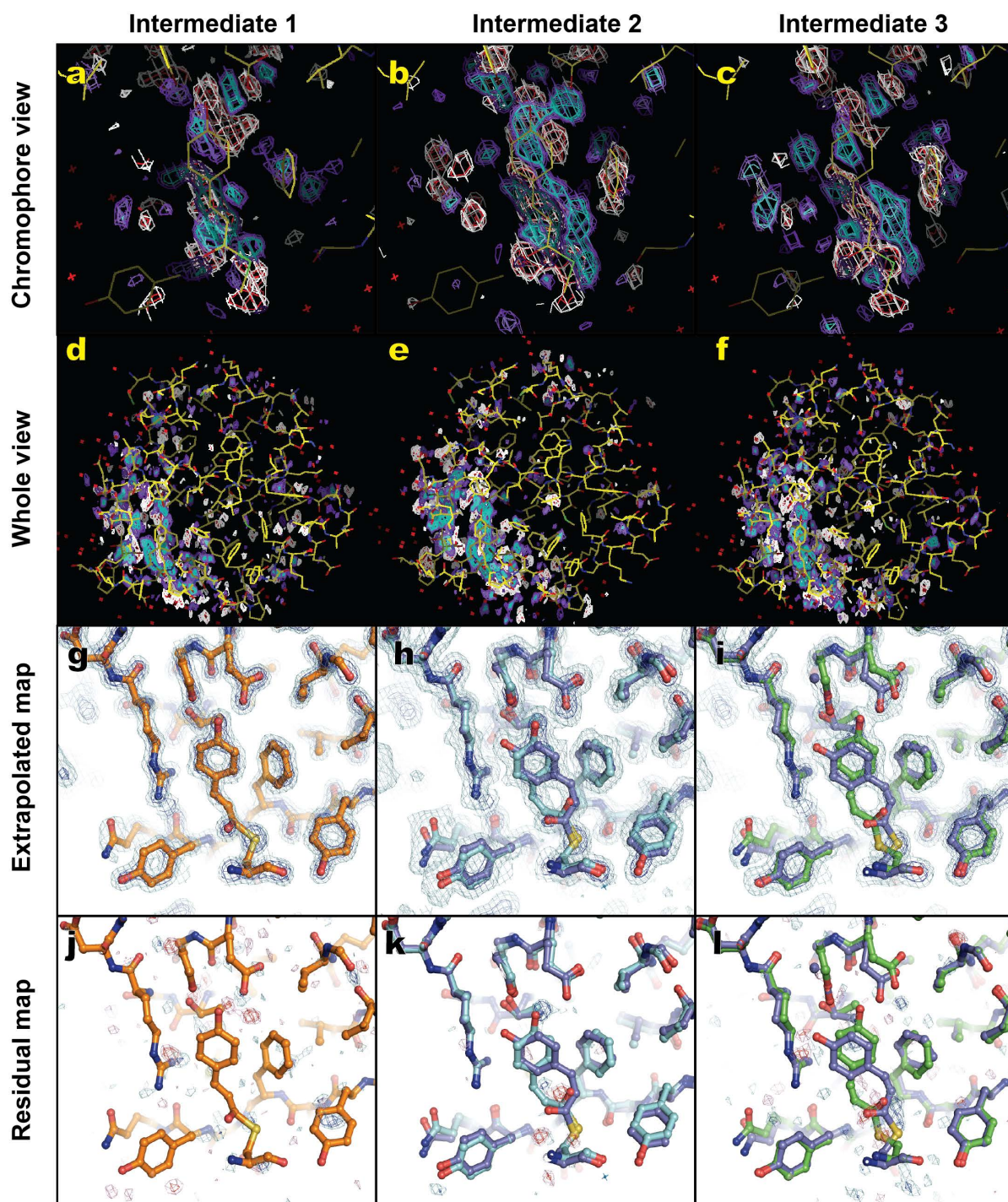
Supplementary Figure S5.



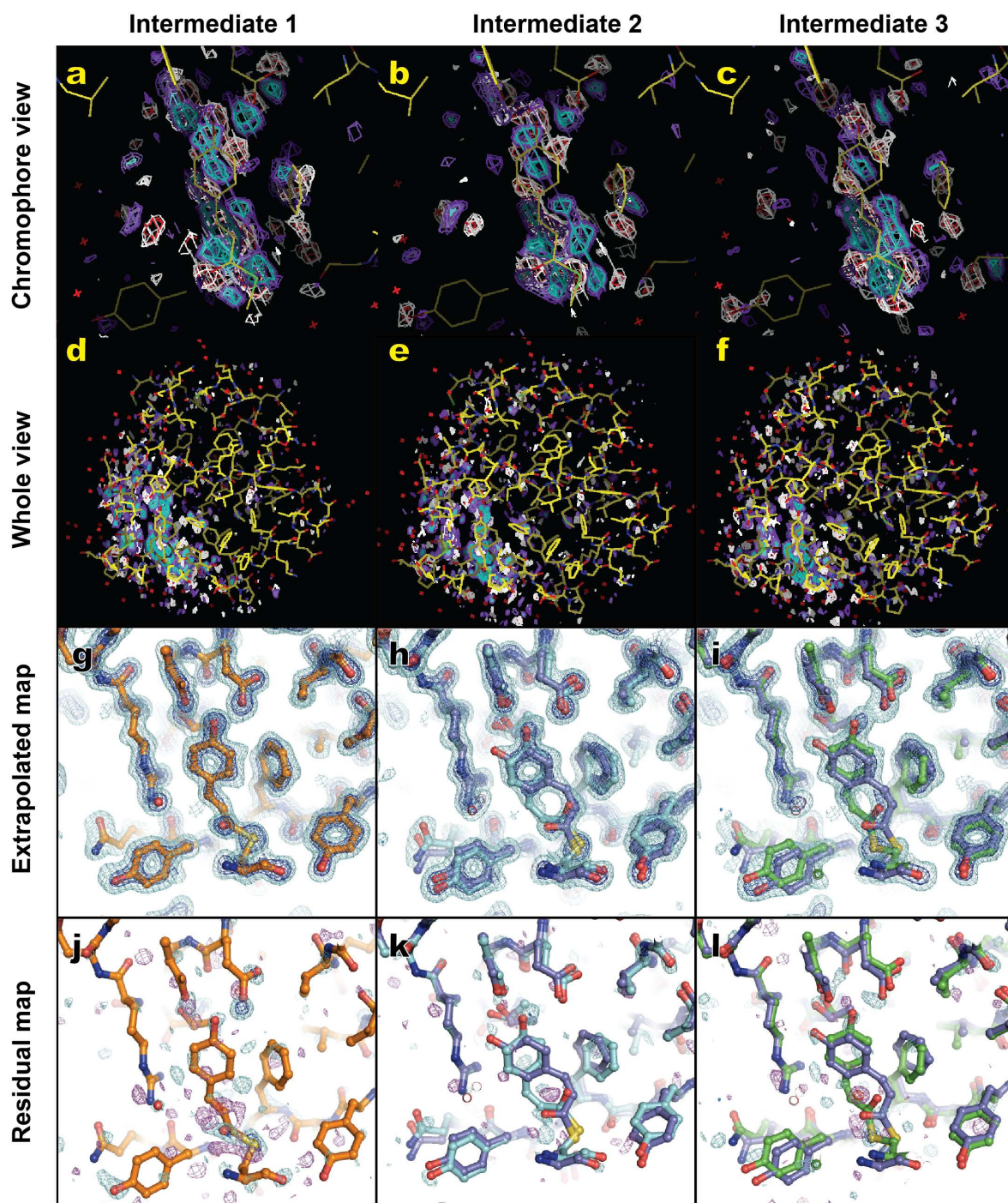
Supplementary Figure S6.



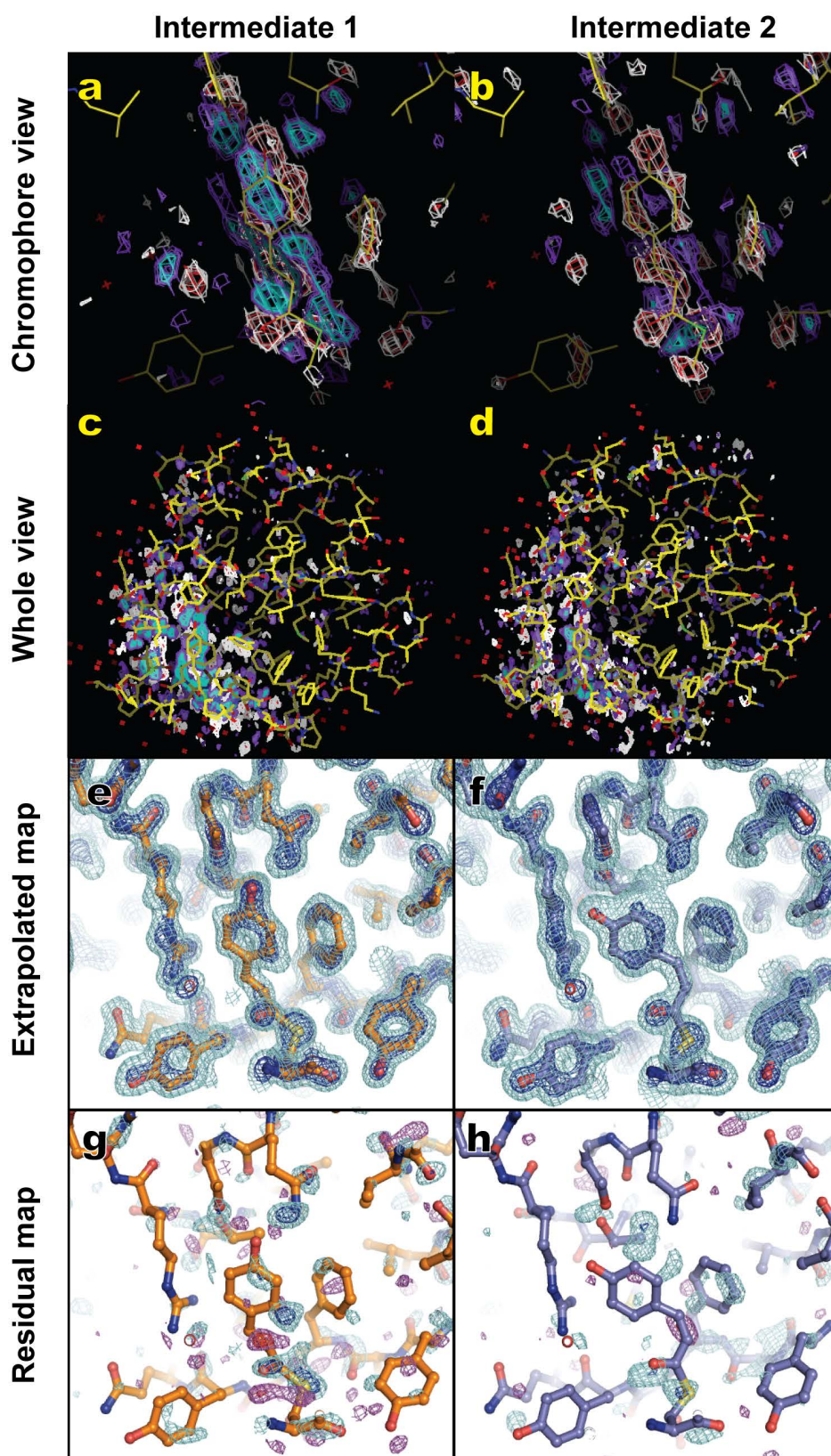
Supplementary Figure S7.



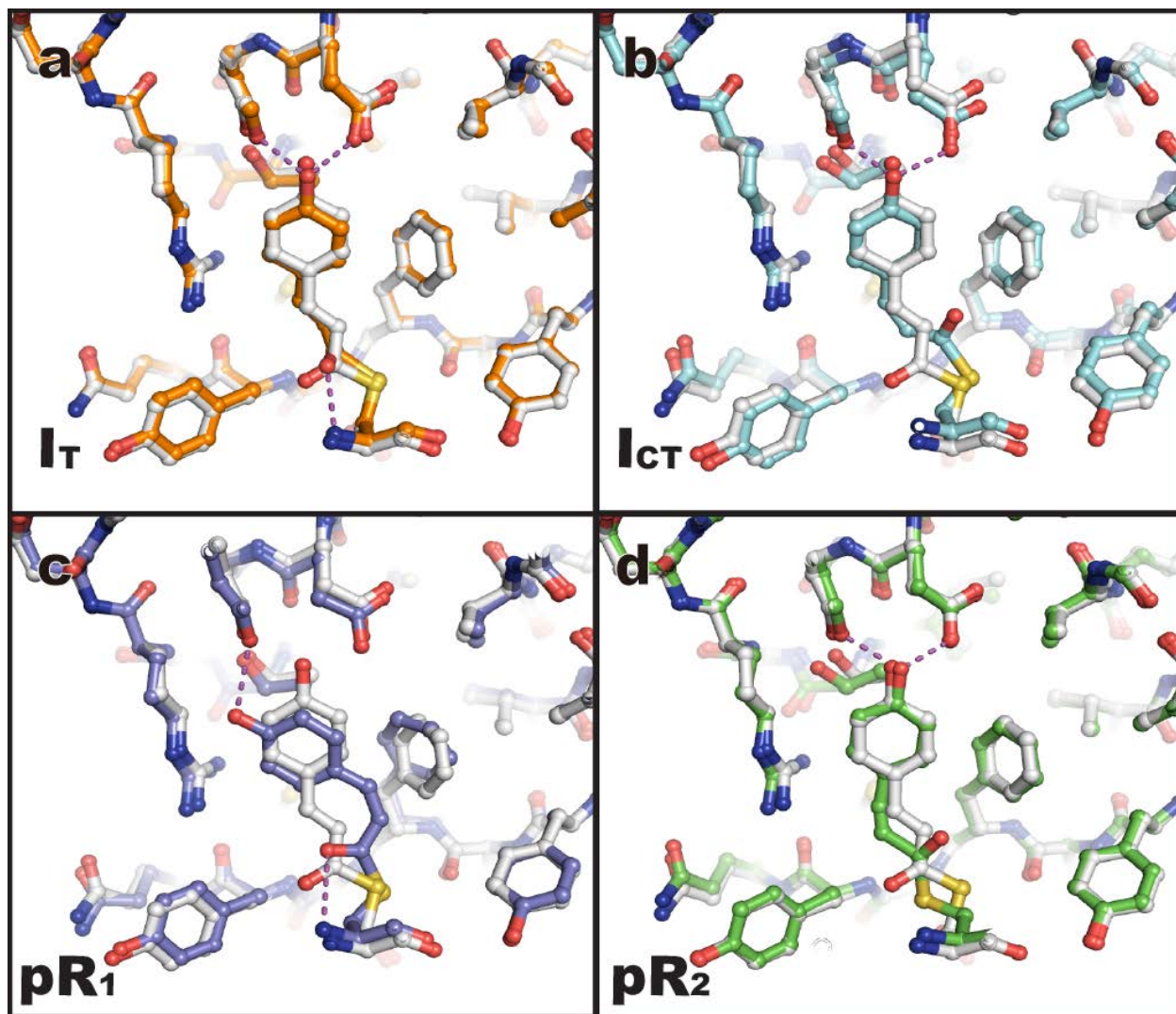
Supplementary Figure S8.



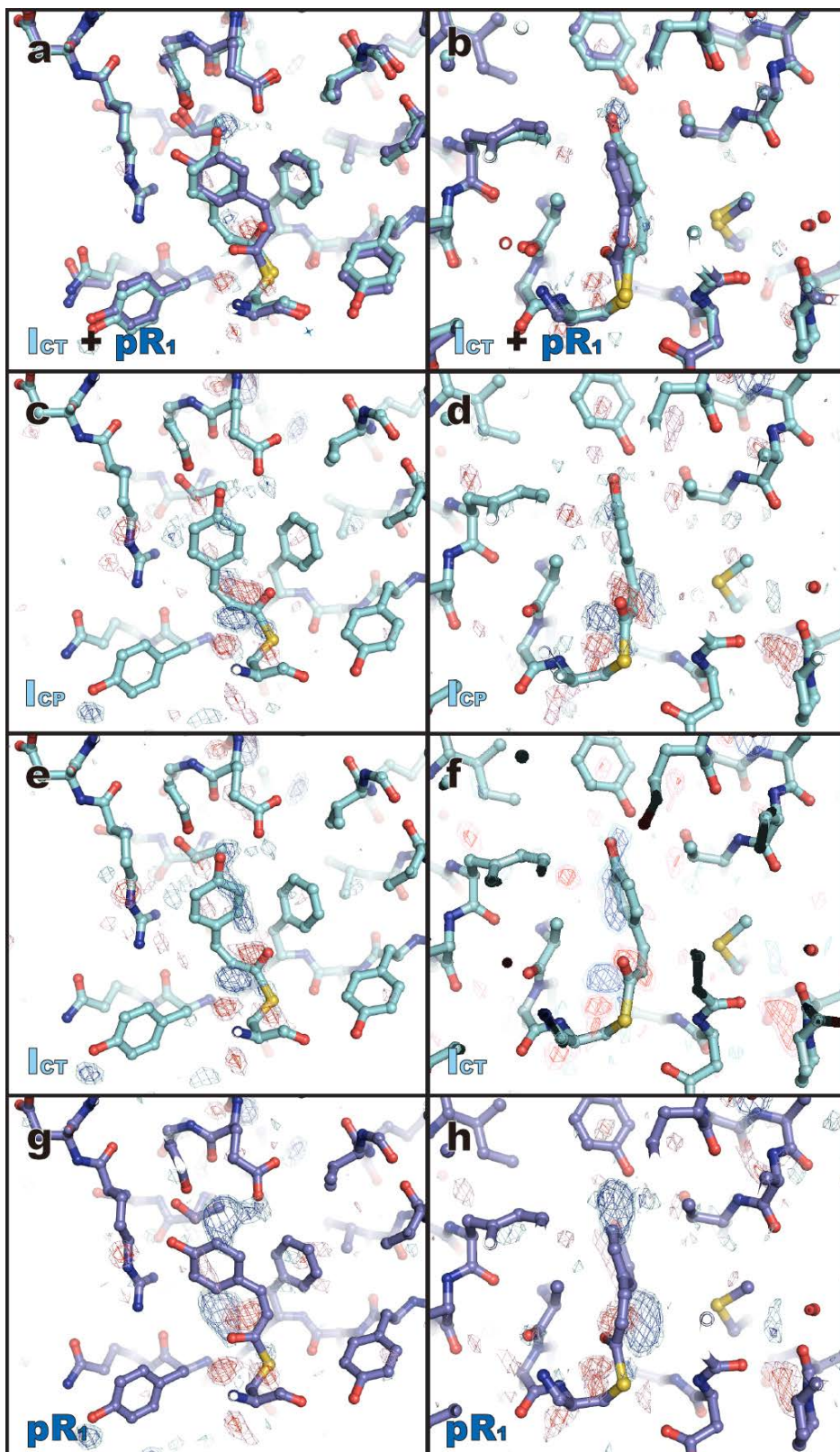
Supplementary Figure S9.



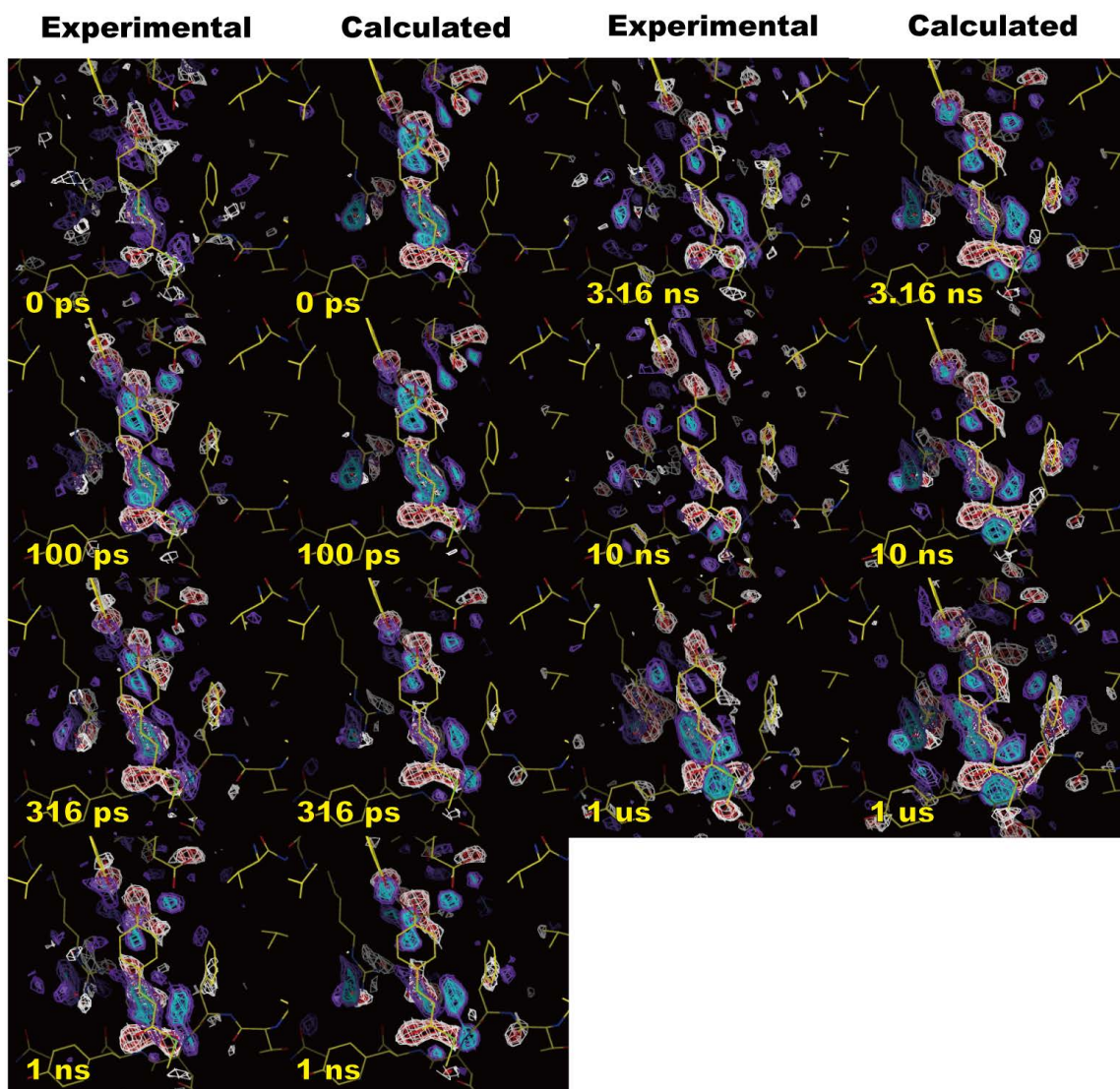
Supplementary Figure S10.



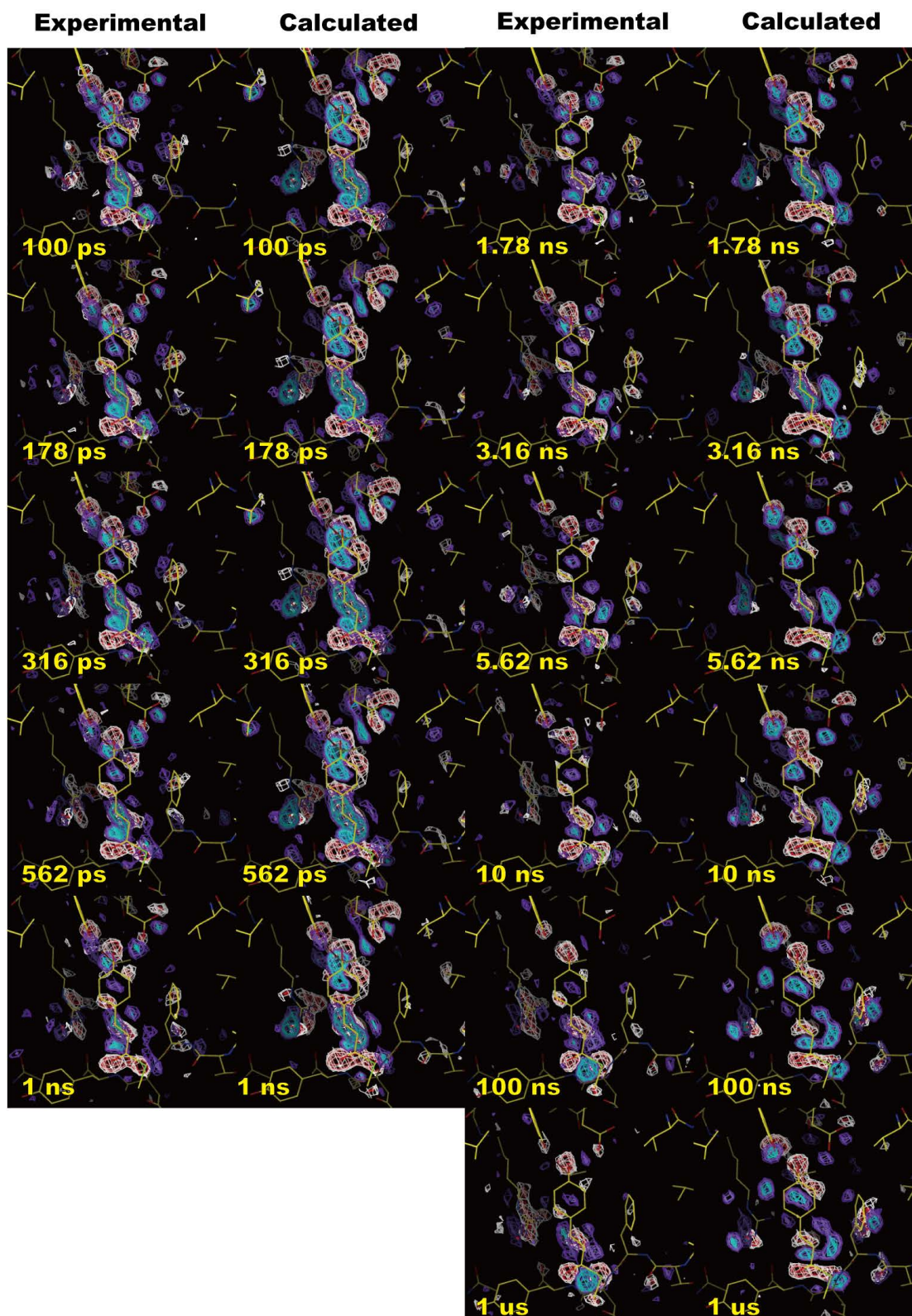
Supplementary Figure S11.



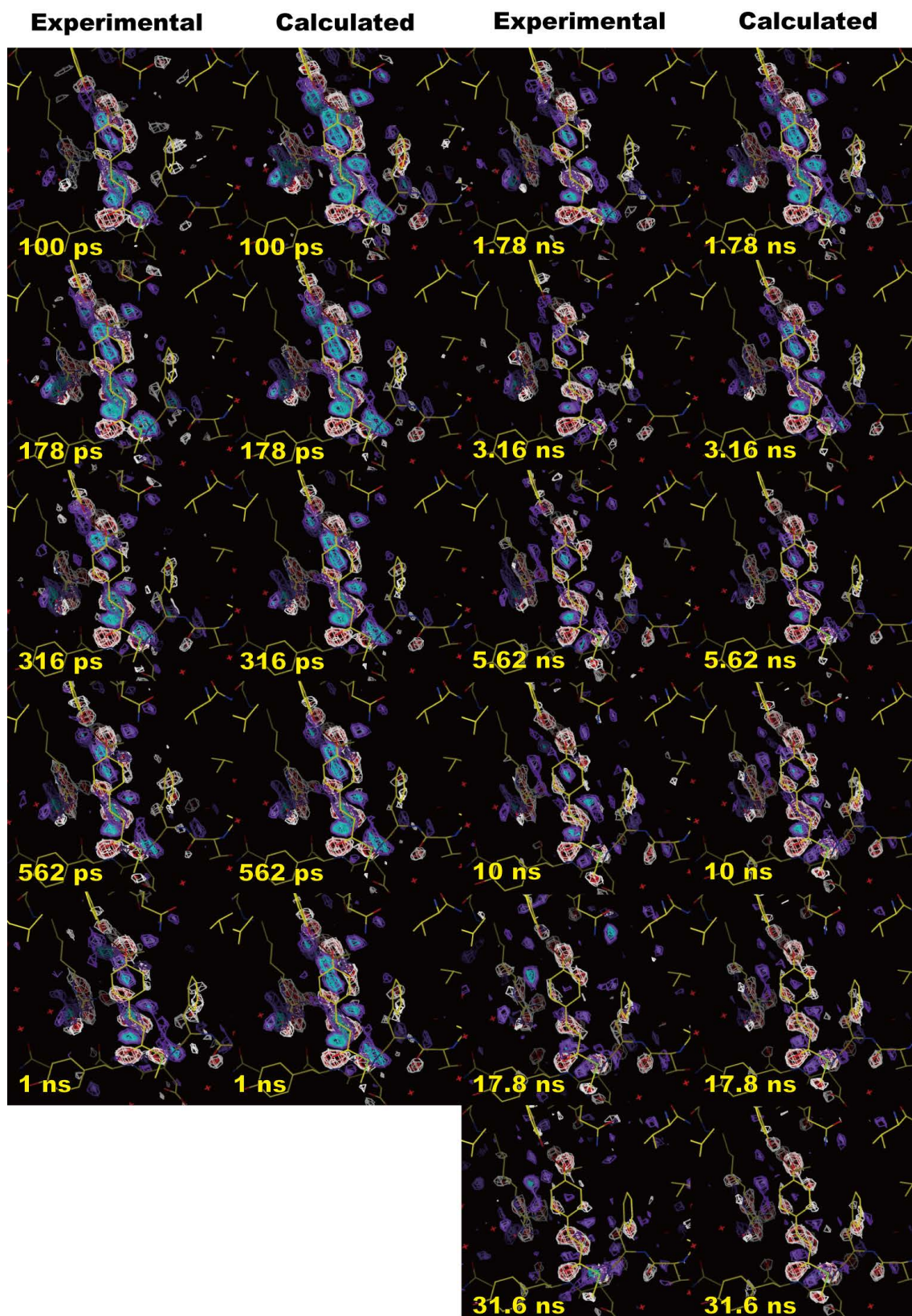
Supplementary Figure S12.



Supplementary Figure S13.



Supplementary Figure S14.



Supplementary Movie captions

Supplementary Movie S1. The evolution of the WT-ESRF electron density distribution in the vicinity of the chromophore binding pocket is shown in frontal (left) and side (right) views. The images were constructed from time-resolved magenta-green density electron density maps at 7 time points (-20ns, 0 s, 100 ps, 316 ps, 1 ns, 3.16 ns, 10 ns and 1 μ s). Maps corresponding to each time point were generated by superimposing experimentally-determined thresholdless electron density maps for the ground state (magenta) and the photoproduct state (green). Magenta and green blend to white; thus, the appearance of color indicates structural change, and the direction of molecular motion follows the magenta-to-green color gradient. Each frame of the movie represents a moving weighted average of the electron density from adjacent time points. The numerical time indicator advances at the mid-point between adjacent time points.

Supplementary Movie S2. The evolution of the WT-APS electron density distribution in the vicinity of the chromophore binding pocket is shown in frontal (left) and side (right) views. The images were constructed from time-resolved magenta-green density electron density maps at 10 time points (-20ns, 100 ps, 178 ps, 316 ps, 562 ps, 1 ns, 1.78 ns, 3.16 ns, 5.62 ns, 10 ns, 100 ns, and 1 μ s). All color schemes are identical to Supplementary Movie S1.

Supplementary Movie S3. The evolution of the E46Q-APS electron density distribution in the vicinity of the chromophore binding pocket is shown in frontal (left) and side (right) views. The images were constructed from time-resolved magenta-green density electron density maps at 10 time points (-20ns, 100 ps, 178 ps, 316 ps, 562 ps, 1 ns, 1.78 ns, 3.16 ns, 5.62 ns, 10 ns, 17.8 ns

and 31.6 ns). All color schemes are identical to Supplementary Movie S1.

Supplementary Movie S4. Isomerization pathways connecting the refined structures found in this study. The bicycle-pedal mechanism is shown in the left panel ($pG \rightarrow I_T \rightarrow I_{CT} \rightarrow pR_2$) and the hula-twist mechanism is shown in the right panel ($pG \rightarrow I_T \rightarrow pR_1$). This movie was prepared using *lsqman*²⁸ and *pymol*²⁹; the atomic coordinates for each frame were interpolated between intermediate structures using the internal morphing method of *lsqman* program. The color scheme for the intermediates follows that of Fig. 4a (pG: gray, I_T : orange, I_{CT} : cyan, pR_1 : blue, and pR_2 : deep green).